# Chapter 6

## *Design of acid bifunctionality (Lewis and Brønsted) on mesoporous silicate, KIT-6 for the conversion of biomass-derived glucose into hydroxymethylfurfural*


# Abstract

A sulfonated Nb-doped KIT-6 catalyst (Nb-KIT-6-$SO_3H$) was successfully synthesized using a hydrothermal self-assembly method, and its performance in producing hydroxymethylfurfural (HMF) from *Saccharum spontaneum* derived glucose and banana peduncle derived glucose was investigated. The physicochemical features of the as-prepared catalysts were characterized by different techniques, including FTIR, p-XRD, SAXS, UV-Vis, $NH_3$-TPD, TGA, BET, XPS, SEM, EDX, and TEM. The results confirm its high ordered cross-linked framework with *Ia3d* symmetry and a high surface area along with promising acidic strength. The impact of different reaction parameters such as catalyst loading, substrate concentration, temperature, and reaction time was investigated using multivariate experimental designs viz., Response Surface Methodology (RSM) and Artificial Neural Network (ANN). The highest HMF yield of ~80% is obtained from glucose with selectivity of ~85% at 150°C after 60 min in MIBK/water (NaCl) solvent system. The catalyst could sustain its good catalytic activity for five consecutive cycles, indicating its high physical-chemical stability. The acidity of Nb-KIT-6(20)-$SO_3H$, the biphasic MIBK-water (NaCl) system, and the tuning of reaction conditions are all aspects that contribute to enhanced glucose dehydration to HMF performance.


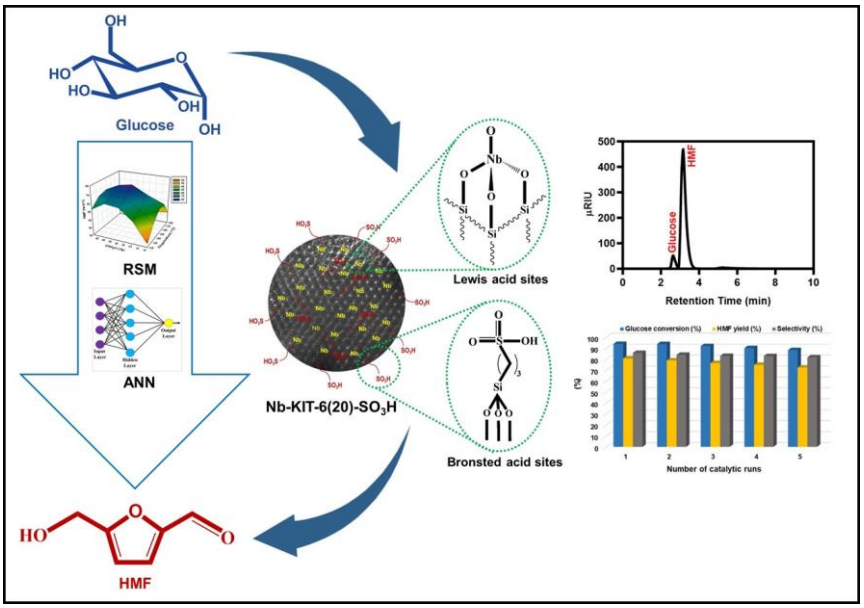

## 6.1. Introduction

The rising concern over global energy shortages, as well as a desire to safeguard the environment, have reawakened the need for renewable energy development. In this context, the dehydration of biomass derivatives to 5-hydroxymethylfurfural (HMF), a potential platform alternative for fuels and fine chemicals, has piqued the interest of researchers in recent years [1]. Simple carbohydrates like glucose and fructose may be transformed to HMF using a variety of acid-base catalysts, both homogeneous and heterogeneous. Fructose may be converted to HMF in a single step over Brønsted acid sites, resulting in a greater yield [2, 3]. However, glucose is preferred over fructose for HMF production due to its low cost and widespread availability [4]. The most commonly reported glucose to HMF pathway involves two steps:

(i) Glucose isomerization to fructose and

(ii) Fructose dehydration to HMF.

The isomerization of glucose is exceedingly difficult, limiting the efficiency of HMF production [5, 6, 7]. A variety of catalysts have been developed for the conversion of glucose to HMF, including metal oxide [8], mineral acid catalysts [9], metal chlorides [10], ionic liquids [11, 12], and solid acid catalysts [13]. Heterogeneous catalysts, on the other hand, are ideal for industrial use due to their separability and reusability.

Heterogeneous solid acid catalysts for the production of HMF include zeolite [14], heteropolyacids [15], acidic carbon [16], polymer resin [17], and acidic mesoporous molecular sieves [18]. Among these, acidic mesoporous molecular sieves have roused the interest of many researchers because of their superior structural features, high surface area, relatively large pore size, and tunable kinds of acidic functional groups [18]. Cao et al. have synthesized a set of solid acid catalysts based on mesoporous MCM-41 silica containing Aluminum and investigated their catalytic activity in a biphasic reaction environment. They observed that the presence of acid sites with significant concentrations was responsible for the successful dehydration of glucose [19]. Likewise, MCM-48 and SBA-15 have gained significant interest in recent years due to their promising applications in catalysis [20]. Transition metal ions were introduced into these materials by a direct hydrothermal synthesis approach, which allows for uniform distribution of the heteroatoms throughout the framework while preventing pore-blockage, which usually occurs when they are included as metal-oxide particles [20]. Besides MCM-41 and SBA-

15 type silicas, recent investigations have demonstrated that transition metals [21, 22] may be readily integrated into KIT-6 structures, which exhibit ordered 3D mesoporous silicate with cubic *Ia3d* symmetry, adjustable pore size, increased wall thickness, and high thermal stability. KIT-6 silica is a porous material comprised of two interconnected mesoporous subnetworks, similar to MCM-48, but with substantially larger mean pore sizes [23]. Jiang et al. synthesized Zirconium doped KIT-6 and found it to exhibit good catalytic activity for the dehydration of glucose to HMF [24].

As solid acid catalysts, Nb-containing porous materials have received a lot of interest. Microporous AM-11 crystalline niobium silicates, for example, have been investigated as solid acid catalysts for the dehydration of xylose [25]. In another study, Nb-containing SBA-15 was found to be active for sucrose hydrolysis [26]. The transesterification of sunflower oil with methanol [27] and Beckmann rearrangement of cyclohexanone oxime [28] was found to be performed by Nb-containing MCM-41. Besides, Nb-incorporated porous silicates show high activity in the epoxidation of propylene [29], cyclohexene [30], and 1-hexene [31] as well as the oxidation of methanol and cyclopentene [32].

Further studies revealed that Lewis acid sites are critical for glucose isomerization and that adequate Brönsted acid sites aid in the production of higher HMF yields during glucose hydrolysis [33]. Developing a highly selective catalytic system with a high HMF yield for the conversion of glucose to HMF thus remains a significant challenge [34, 35]. Mohammadbagheri et al. employed propyl sulfonic acid to graft fibrous nanosilica to enhance the active sites of the catalyst for the conversion of furfuryl alcohol to n-butyl levulinate [36]. Similarly, methyl propyl sulfonic acid-functionalized MCM-41 was also assessed in the conversion of xylose to furfural [37].

Taking into account the background of the published literature mentioned above, we have focused on the development of a propyl-sulfonic acid sulfonated Nb-KIT-6 catalyst, through a one-pot synthesis approach for the generation of HMF from biomass-derived glucose. The catalytic performance of the catalyst was investigated using different solvent systems. The structure, morphology, and physiochemical properties of the catalysts are characterized using FT-IR, p-XRD, SAXS, TGA, Diffuse reflectance UV-Vis, $NH_3$-TPD measurements, $N_2$ adsorption-desorption isothermal analysis, XPS, SEM, EDX, and HRTEM analysis. The reaction parameters affecting the yield of HMF such as temperature, reaction time, catalyst loading, and substrate concentration were optimized

using multivariate experimental designs viz., Response Surface Methodology (RSM) and Artificial Neural Network (ANN), as well as the reusability of the catalyst, was investigated. A probable reaction mechanism over the catalyst was also hypothesized based on the findings.

## 6.2. Experimental section

### 6.2.1. Materials

Tetraethyl orthosilicate (TEOS) (98%, Merck India Pvt. Ltd.) and Niobium pentachloride ($NbCl_5$) (Acros organics) were used as silicon and niobium sources, respectively. Triblock copolymer Pluronic P123 ($EO_{20}$-$PO_{70}$-$EO_{20}$, Mw~5800) was used as a structure directing agent and n-Butanol (SRL) as a co-solvent. HMF (as a standard sample for HPLC analysis) and 3-Mercaptopropyltrimethoxysilane (MPTMS) were purchased from Merck India Pvt. Ltd. Tetrahydrofuran (THF), Methylisobutylketone (MIBK), *N*-Methylpyrrolidone (NMP), Dimethylformamide (DMF) and Dimethylsulfoxide (DMSO) were purchased from Sisco Research Laboratories Pvt. Ltd. (SRL). All other chemicals, which were of an analytical grade, were applied without further purification.

### 6.2.2. Synthesis of mesoporous Nb-KIT-6

Niobium-doped KIT-6 (Nb-KIT-6) has been synthesized using Pluronic 123 and n-Butanol as the structure-directing agents. In a typical synthesis method, 4 g of Pluronic P123 was dissolved in 144 ml of distilled water with 7.4 ml of HCl (37 wt%) under 35°C for 4 h. 5 g n-Butanol was then added after complete dissolution of the solution and the resulting mixture was stirred for another 1 h at 35°C. Following that, 8.6 g of TEOS and the requisite quantities of $NbCl_5$ were slowly added to the mixture, and it was stirred for another 24 hours. Thereafter, the reaction mixture was hydrothermally treated for 24 h at 100°C after transferring to a 300 mL Teflon-lined SS autoclave. Finally, the white precipitate obtained was filtered without washing and then oven dried at 100°C for 12 h. The dried product was finely powdered using a mortar pestle and then calcined at 550°C for 6 h to obtain Nb-KIT-6. Using the similar synthetic procedure, the quantity of $NbCl_5$ was varied and the samples were denoted as Nb-KIT-6(x), where x was the molar ratio of Si/Nb. Pure silica KIT-6 has also been synthesized following the same procedure without the addition of $NbCl_5$ for reference.

### 6.2.3. Preparation of functionalized mesoporous Nb-KIT-6

The as-prepared Nb-KIT-6 was functionalized with sulfonic acid groups *via* co-condensation method. For this, 1 g of Nb-KIT-6 was added to a mixture containing 30 ml of dry toluene and 1 ml of MPTMS and then refluxed at 130°C for 24 hours with stirring. The resulting thiol functionalized solid product was filtered thoroughly and extracted using methanol in a soxhlet system for 12 h before putting in an oven to dry overnight at 80°C. Subsequently, the thiol groups were oxidized into $–SO_3H$ groups by 50 ml of $H_2O_2$ under continuous stirring for 24 h at room temperature. The functionalized product was then filtered, washed thrice with methanol, and oven dried at 80°C for 12 h. The resulting product was denoted as Nb-KIT-6(x)-$SO_3H$ (Fig. 6.1).

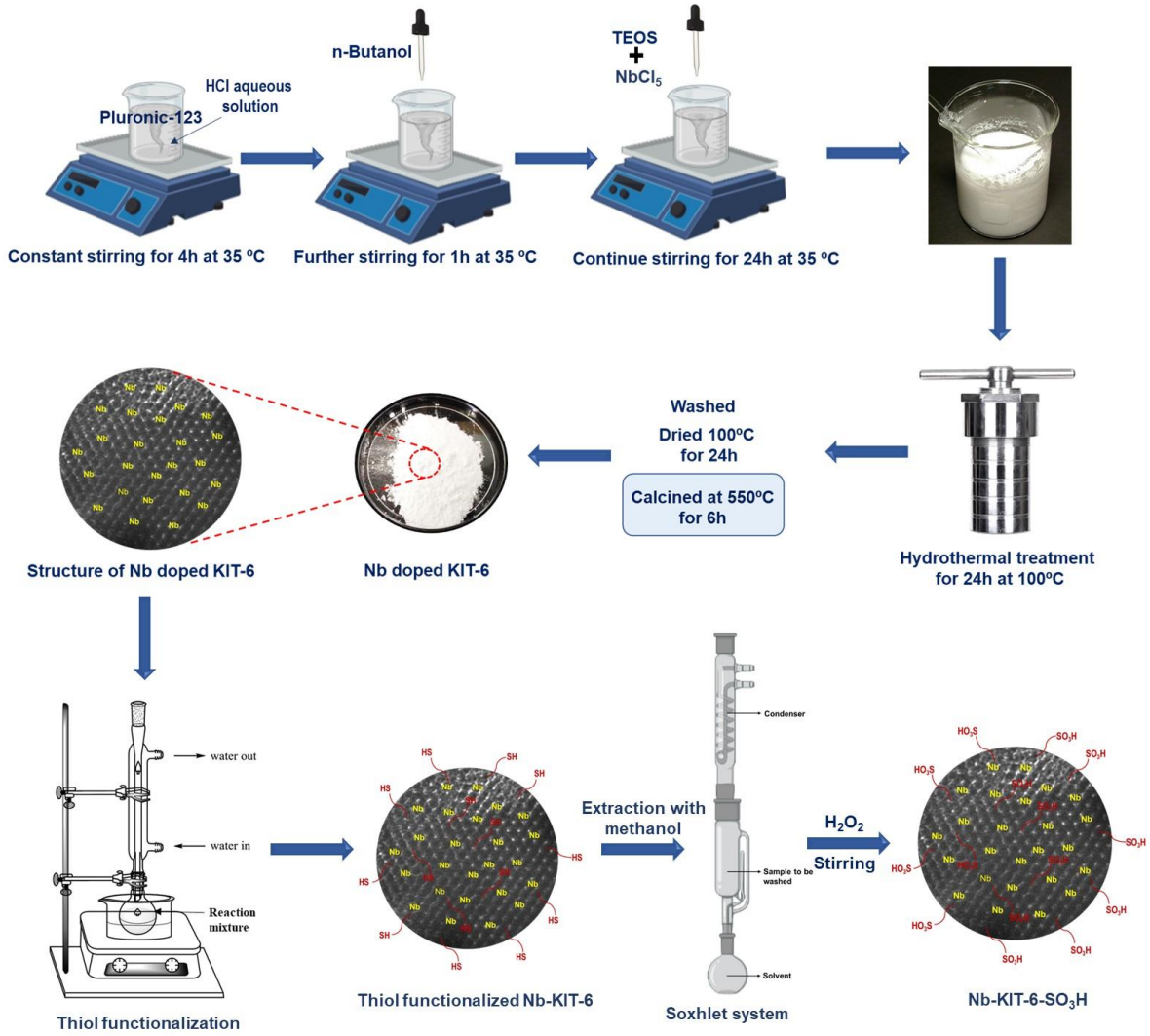


***Fig. 6.1.*** *Schematic representation of the synthetic procedure of Nb-KIT-6-$SO_3H$ catalyst.*

### 6.2.4. Catalysts characterization

Fourier transform infrared (FT-IR) spectra were obtained in the Potassium Bromide (KBr) medium on a Perkin Elmer Spectrum 100 Optica FT-IR Spectrometer (USA). Typically, 5 mg of synthesized sample were ground with 95 mg pure KBr (5:95 w/w ratio) and pelletized with the help of a Qwik Handi-Press Kit. The KBr disc was then mounted in a quartz IR cell and read in the wavelength range of 500–4000 $cm^{-1}$ with 32 scans at an effective resolution of 4 $cm^{-1}$, for each sample.

Powder X-ray diffraction patterns (p-XRD) of the synthesized samples were recorded using an X-ray Diffractometer (Rigaku-Miniflex, Japan) with Ni filtered Cu Kα radiation ($\lambda$ = 1.5406 Å) at the operating voltage and current of 40 kV and 15 mA respectively. Each sample was scanned over the 2θ range of 10°∼50° and a scan rate of 1° $min^{-1}$. The 3-D structure of KIT-6 was evaluated by Small Angle X-ray Scattering (SAXS) patterns on SAXS point 2.0, Anton Paar where the small-angle from 0.5°~5° was chosen with Cu Kα radiation (λ = 1.5405 Å).

The thermal stability of the catalysts was analyzed by thermogravimetric analysis (TGA) with respect to weight loss due to an increase in temperature. The analysis was performed by an STA 6000 Simultaneous Thermal Analyzer from Perkin Elmer (USA). For the analysis, the samples were gradually heated from room temperature to 700°C at a heating rate of 20°C $min^{-1}$ in an ambient nitrogen environment.

The acidities of the prepared catalysts were investigated using $NH_3$-Temperature programmed desorption ($NH_3$-TPD) analysis. The analysis was performed on a Micromeritics, AUTOCHEM - 2950 instrument. At first, the catalyst was degassed for 1 hour at 150°C with a flow rate of 30 mL $min^{-1}$ of He gas. The degassed sample was then saturated with $NH_3$ at a flow rate of 30 ml $min^{-1}$ for 40 min at 50°C. The sample was then heated for 1 hour at 100°C with a flow of He (30 mL $min^{-1}$) to remove any physisorbed $NH_3$ from the catalyst surface. Finally, the $NH_3$ desorption was monitored and the data was recorded on a thermal conductivity detector linked to a chemisorption device in the temperature range of 100°C to 800°C.

The surface area, pore size, and pore volume of the catalysts were calculated using Brunauer-Emmett-Teller (BET) method measured by $N_2$ physisorption with a Quantachrome Instruments (NOVA 1000e). The measurement of X-ray photoelectron spectroscopy spectra was performed on an X-ray photoelectron spectrometer (Thermo Fisher Scientific Pvt. Ltd., ESCALAB Xi+, UK).

Morphology study and elemental distribution of the catalyst were examined by a Scanning Electron Microscope (SEM) (JSM-6390, JEOL, Singapore) and SEM-EDX (SEM-Energy Dispersive X-ray Diffraction spectroscopy), respectively. Pseudo-colors were used to generate the Elemental map to illustrate the elemental distribution in the synthesized catalyst. The morphology of the synthesized catalyst was further analyzed using transmission electron microscopy (FEI company, USA). For this, the sample was ground in an agate mortar, and a small amount was dispersed in anhydrous ethanol, which was dispersed using ultrasound. The suspension was then absorbed by a capillary tube into the copper network with carbon film suspended. After drying, it was observed in the electron microscope chamber. Their average dimensions were determined from the TEM images using the Image J (NIH) processing suite.

### 6.2.5. Reaction procedure using Multivariate Experimental Design

All the catalytic glucose conversion reactions were performed in a 50 ml round bottom flask located in a temperature-controlled oil bath and equipped with a magnetic stirring bar. In a typical experiment, an appropriate amount of glucose and catalysts were loaded into the flask along with a 5 mL solvent, and the reaction mixture was vigorously stirred at 300 rpm at a specific reaction temperature for a given reaction time (according to the experimental design). After completion of the reaction, the mixture was immediately put into ice water and cooled to room temperature. The catalyst was then separated by centrifugation and then filtering the solution through a 0.2 m syringe filter.

*Response surface methodology:*

RSM statistical approach was used to investigate the effect of independent experimental factors on glucose dehydration reaction while also achieving the optimum reaction condition [38, 39]. For this, the effects of univariate and multi-variate interactions among the experimental factors (temperature, reaction time, catalyst loading, and substrate concentration) on HMF yield were studied through RSM based on Central Composite Design (CCD). A total of 21 experiments were considered for the quadratic model with four components and five levels. The statistical software package, Design-Expert 7.0 (Stat-Ease Inc., USA) was used to do the analysis of variance (ANOVA), regression analysis, design of experiment, and graphical analysis. The dehydration reaction data was modeled using the second-degree polynomial equation given below to reflect the relationship between the predicted response and experimental components [40].

$$Y = b_0 + \sum_{i=1}^{n} b_i X_i + \sum_{i=1}^{n} b_{ii} X_i^2 + \sum_{i=1}^{n} \sum_{i>j}^{n} b_{ij} X_i X_j$$

where n is the total number of variables, $X_i$ and $X_j$ are the coded values, $b_0$ is the model constant, Y is the predictive response, $b_{ii}$ is the interaction coefficients, $b_i$ is the linear coefficient, and $b_{ij}$ is the quadratic coefficient.

*Artificial Neural Networks modeling:*

The RSM dataset was then combined with a three-layer feed-forward Multi-Layered-Perceptron (MLP) utilizing an artificial neural network (ANN) *via* MATLAB R2019b computer suite (MathWorks USA) to predict the influence of multivariate associations under various reaction conditions on HMF yield. The network consists of three layers: an input, a hidden, and an output layer. A Levenberg Marquardt (LM) back-propagation learning system with tan sigmoid function (tansig) in the hidden layer and linear transfer function (purelin) in the output layer along with the neuron numbers in the input and output layers determined by the relative importance of the parameters detected in RSM dataset was used to create the neural system.

*Model performance indices*

To choose the best predictive model for the investigational data, the performance metrics of RSM and ANN modeling predictions were employed. Table 6.8 shows the results of the analysis, which employed seven statistical error functions that performed well. The assessment indices used were evaluated based on the information set used [41]. Furthermore, a relative parity map was employed to show specific deviation sites between RSM and ANN model estimates based on the investigative data.

### 6.2.6. Substrate and product analysis

The substrate and the reaction product were analyzed using high-performance liquid chromatography (HPLC, Thermoscientific) equipped with an Accucore Hilic Amide column (150 X 4.6 mm) and a RI detector. A volume of 20 µl of the samples was injected into the column at a temperature of 65°C through the mobile phase of 0.5 mM $H_2SO_4$ at a flow rate of 0.6 mL per minute. Calibration curves obtained from standard glucose solutions and standard HMF solutions run under similar experimental conditions were used to calculate the glucose and HMF concentration.

The carbohydrates conversion, the HMF selectivity, and yield were evaluated by using the following equation.

$$\text{Conversion of glucose (\%)} = \frac{[Carbohydrates] \times V - [Carbohydrates]' \times V}{[Carbohydrates] \times V} \times 100$$

$$\text{Yield of HMF (\%)} = \frac{[C] \times V}{[Carbohydrates] \times V} \times \frac{M_a}{M_b} \times 100$$

$$\text{HMF Selectivity (\%)} = \frac{Yield}{Conversion} \times 100$$

where [Carbohydrates] was the initial concentration of carbohydrates in solution; [Carbohydrates]' was the finial concentration of carbohydrates in solution; [C] was the finial concentration of HMF. V was the volume of the mixture solution; $M_a$ was the molecular weight of glucose; $M_b$ was the molecular weight of HMF.

### 6.2.7. Catalyst reusability test

The stability of the Nb-KIT-6-$SO_3H$ catalyst was tested by reusing the recovered catalyst in a series of experiments. After each run, the catalyst was separated by centrifugation, thoroughly washed with methanol, and then dried in a hot-air oven at 80°C. The reaction for each cycle was carried out under the optimal conditions obtained using a multivariable experimental design. The spent catalyst obtained after the last experimental run was analyzed using FTIR, TGA, and SEM-EDX techniques to study the stability test.

## 6.3. Results and discussion

### 6.3.1. Comparison of catalytic activity of different synthesized catalysts and in different solvents based on HMF yield

At first, the synthesized Nb-KIT-6-$SO_3H$ catalyst was evaluated along with pure silica KIT-6 and non-functionalized Nb-KIT-6 catalysts based on glucose conversion and HMF yield under a specific reaction condition (Fig. 6.2 a). All the primary reactions are carried out in a biphasic solvent system (MIBK-saturated NaCl) at 120°C for 60 min. From Fig. 6.2 a it is observed that the catalytic activity of KIT-6 catalyst was very poor resulting in only 18.3% glucose conversion and a total of 3.13% HMF yield. KIT-6 catalyst, on the other hand, demonstrated high efficiency when doped with Nb (Nb-KIT-6) with 70.83% glucose conversion and 44.91% HMF yield. The relatively low yield of KIT-6 might be

due to the lack of Lewis/Brønsted acidic sites, which are essential to drive the reaction, whereas Nb-KIT-6 demonstrated a considerable product yield, confirming the involvement of Nb in the reaction. When Nb-KIT-6 was further functionalized with sulfonic acid groups, the corresponding Nb-KIT-6-$SO_3H$ catalyst exhibited a considerable improvement in glucose conversion (91.43%) as well as HMF production (70.03%).

Fig. 6.2 b shows the effect of the molar ratio of Si/Nb loading on the catalytic activity of Nb-KIT-6(x)-$SO_3H$ catalysts. Both the glucose conversion and HMF yield increase if Nb is doped into the KIT-6 catalyst as discussed earlier. Nb-KIT-6(20)-$SO_3H$ presents the highest activity among all the studied Si/Nb ratio (viz., 5, 10, 20, and 30) where ~90% glucose conversion was observed along with 70.21% HMF yield. However, further raising the molar ratio to 30 resulted in a slight reduction in HMF production, which might be ascribed to HMF being converted to other by-products at high acid density. Taking all these aspects into account, it was determined that the Nb-KIT-6(20)-$SO_3H$ catalyst was better suited for HMF production and was employed to further investigate the reaction parameters.

A number of single-phase and two-phase solvents with varying ratios were used in the reaction to examine the effect of solvents in the glucose conversion processes. The yields of HMF seemed to fluctuate in several monophasic solvents, indicating a significant solvent effect **(**Fig. 6.2 c). After the reaction at 120°C for 60 min, the yield of 5-HMF in the monophasic solvents was considerably lower than that in the biphasic solvents. With MIBK as the solvent, Nb-KIT-6(20)-$SO_3H$ had poor catalytic activity, which might be due to the decreased solubility of the substrate. Glucose conversions were quite high in THF, BuOH, and DMF due to the high solubility of reactants, however, the poor 5-HMF yield was due to the presence of side reactions and the creation of humins [42]. The glucose conversion and HMF yield in NMP and DMSO reached > 95% and > 60%, respectively, suggesting that Nb-KIT-6(20)-$SO_3H$ possessed a stable catalytic activity in both the solvents. But their selectivity (66.21% and 65.56%) is low compared to the biphasic systems. In the biphasic solvent containing MIBK and saturated NaCl water 70.45% HMF yield was obtained with a selectivity of 76.18%. In a biphasic reaction system, HMF was generated progressively in the inorganic phase with continuous extraction into the organic phase to accomplish substrate and product separation and as a consequence, it significantly facilitated the HMF yield [43].

Fig. 6.2 d depicts the influence of the inorganic phase to organic phase ratio on the HMF yield. Glucose conversions and HMF yields were poor in MIBK or single-phase saturated NaCl solvents indicating that the presence of both reactants and products in the same phase leads to condensation reactions. The 5-HMF yield in MIBK was greater than that in saturated NaCl solution, demonstrating that organic solvents may hold more 5-HMF molecules than inorganic solvents. To summarise, the optimal volume ratio of MIBK and saturated NaCl solution (4:1) was determined by comparative investigations.

The reason for adding NaCl instead of pure water is because $Cl^-$ has a salting-out effect in the solution and can substantially accelerate the reaction rate, therefore enhancing the separation rate of 5-HMF [44]. To investigate the effect of NaCl on the reaction further, a variety of solvents with varying NaCl concentrations were utilized in the glucose conversion reactions (Fig. 6.2 e). Notably, increasing the NaCl content in the aqueous phase increased the HMF yields in the organic phase. It is believed that the saturated NaCl solution augmented the association of molecular bonds in the liquid components and enhanced the immiscibility of the aqueous and organic phases, consequently increasing the distribution coefficient of HMF in organic phases.

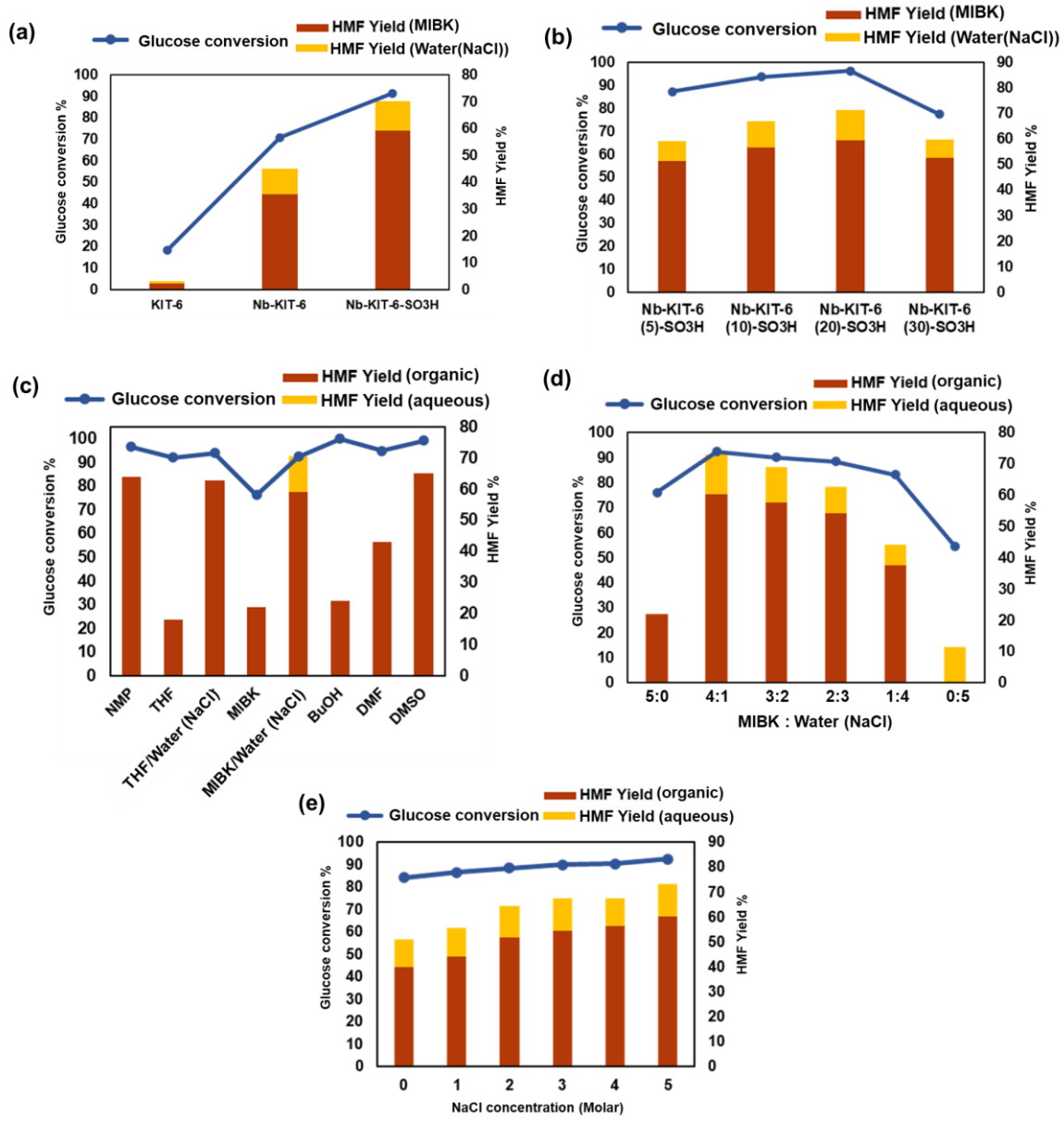


***Fig.6.2.*** *Comparative analysis of the catalytic activity of Nb-KIT-6-$SO_3H$ with pure silica KIT-6 and non-functionalized Nb-KIT-6 (a), the effect of molar ratio of Si/Nb loading on the catalytic activity of Nb-KIT-6(x)-$SO_3H$ catalysts (b), effect of different single-phase and biphasic solvents on the glucose conversion and HMF yield (c), the influence of the inorganic phase to organic phase (MIBK) ratio on the glucose conversion and HMF yield (d), and influence of NaCl concentrations on the glucose conversion and HMF yield (e). (Reaction conditions: 40 mM glucose, 40 mg catalyst, 120°C, 60 min).*

### 6.3.2. Catalysts characterization

The changes in bonding features induced by doping and functionalization of KIT-6 were monitored by FTIR spectroscopy. Fig. 6.3 a represents the FTIR spectra of KIT-6, Nb-KIT-6 with Si/Nb ratio 20, and Nb-KIT-6(x)-$SO_3H$, where x is the Si/Nb ratio. In general, the broad band at around 3460 $cm^{-1}$ and the narrow band at around 1639 $cm^{-1}$ in all the materials are ascribed to stretching and bending vibrations, respectively of O-H in the sample surface water or hydroxyl groups. In the spectra of pure silica KIT-6, the wide band at 1084 $cm^{-1}$ is attributed to asymmetric Si-O-Si stretching mode and the narrow band at 960 $cm^{-1}$ corresponds to Si-OH group vibration [24]. These bands broaden and the intensities decrease in the Nb-KIT-6 spectra, while the intensity further decreases in the sulfonated Nb-KIT-6(x)-$SO_3H$ samples. The symmetric stretching mode of Si-O-Si occurs at 802 $cm^{-1}$, whereas the bending Si-O-Si mode occurs at 460 $cm^{-1}$ in all the spectra. However, these bands are also seen to broaden and weaken on Nb-loading. A distinctive peak at around 945 $cm^{-1}$ is ascribed to the stretching vibration of Si-O-S, signifying the existence of sulfonic acid groups [43].

High-angle p-XRD patterns of all the synthesized samples are presented in Fig.6.3 b. In all cases, the broad peak in the range of $2\theta = 20°$- 24° is ascribed to the amorphous nature of $SiO_2$ [45]. Notably, Nb-KIT-6 with Si/Nb ratio 20 and Nb-KIT-6(20)-$SO_3H$ showed similar patterns to KIT-6, indicating that no evident structural change occurred after the Nb loading and functionalization process. On the other hand, reflections corresponding to $Nb_2O_5$ are observed at high Nb loaded samples viz., Nb-KIT-6(5)-$SO_3H$ and Nb-KIT-6(10)-$SO_3H$. The noticeable shoulder peaks at around 25°-30°, 36°, 47°, and 55° in Nb-KIT-6(5)-$SO_3H$ and Nb-KIT-6(10)-$SO_3H$ are assigned to the crystalline orthorhombic $Nb_2O_5$ (JCPDS no. 30-0873), located at the extra-framework of the catalysts [46]. This is due to metal species aggregation at higher metal loadings, resulting in metal oxide clusters. Although Nb-KIT-6(20)-$SO_3H$ and Nb-KIT-6(30)-$SO_3H$ show similar p-XRD patterns, Nb-KIT-6(20)-$SO_3H$ is the well-suited catalyst in this regard confirming the appropriate metal loading in the porous structure of KIT-6 as evidenced by the catalytic activity results (as discussed in Section 6.3.1).

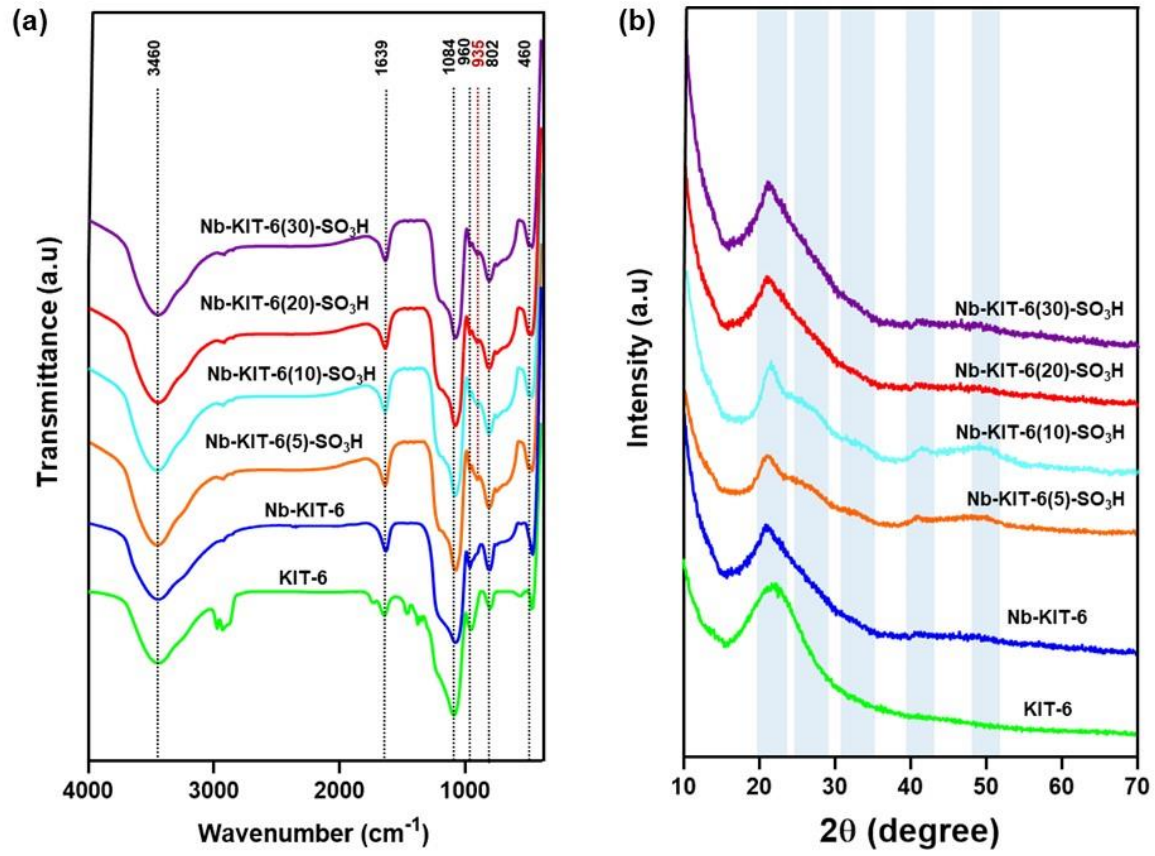


***Fig. 6.3.*** *FTIR spectra (a) and p-XRD patterns (b) of KIT-6, Nb-KIT-6 with Si/Nb ratio 20 and Nb-KIT-6(x)-$SO_3H$ samples, where x is the Si/Nb ratio.*

Fig. 6.4 a shows the SAXS spectra of Nb-KIT-6 and Nb-KIT-6(20)-$SO_3H$ compared with the bare KIT-6. The SAXS pattern of KIT-6 displays notable structural order and symmetry coherent with a body-centered cubic *Ia3d* space group, which is consistent with the data reported in [47], where the main cubic (211) reflection at 2θ = 0.86° and several higher-order diffractions in the region 2θ = 1.4–1.7° confirmed the structural regularity. As seen by the well-resolved diffraction peaks in the SAXS diffraction patterns of Nb-KIT-6 and Nb-KIT-6(20)-$SO_3H$, the ordered pore structure was retained despite the metal loading and sulfonic acid group functionalization. However, with loading and functionalization, the peaks become weak in intensity. Furthermore, a slight shift of the (211) reflection peaks to lower 2θ values was observed after Nb loading and in the functionalized catalyst. This is due to an increase in the unit cell parameter ($a_0$) generated by the inclusion of a larger ionic radius of Nb ions in the KIT-6 framework [48].

The nature and coordination states of the integrated Nb species inside the KIT-6 framework were determined using diffuse refraction UV-Vis spectroscopy. The tetrahedral

coordination of silicate units is required by metal atoms that replace Si atoms isomorphously in the framework of KIT-6. As a result, its UV-Vis adsorption could be distinguished from that of extra-framework species [44]. As shown in Fig. 6.4 b, all the Nb-KIT-6(x)-$SO_3H$ samples exhibit a band centered at around 205 nm. This is generally associated with Nb-O bonds and is attributed to ligand-to-metal charge transfer transition in the $NbO_4$ tetrahedra units resulting from the valence band excitation of an oxygen 2p electron to the vacant orbital of the $Nb^{5+}$ ions of $NbO_4$ tetrahedra units. Besides, all the UV-Vis spectra have an absorption band in the 230-270 nm range which was greatly broadened at higher Nb loading and is probably due to the presence of more than one Nb species. It has been reported that the transition with maxima around 230 and 270 nm ascribed to monomeric and oligomeric $NbO_4$ tetrahedra, was found for evenly dispersed niobium oxide on silica [20]. Furthermore, an absorption band at 330 nm was observed in Nb-KIT-6(5)-$SO_3H$ and Nb-KIT-6(10)-$SO_3H$ spectra that indicate the presence of bulk crystalline $Nb_2O_5$ clusters in the framework of KIT-6 [20]. Hence, we can establish the existence of isolated well-dispersed $NbO_4$ tetrahedral units along with oligomeric $NbO_4$ units in the KIT-6 framework at lower Nb loadings. These findings are consistent with those obtained from the high-angle p-XRD analysis described earlier.

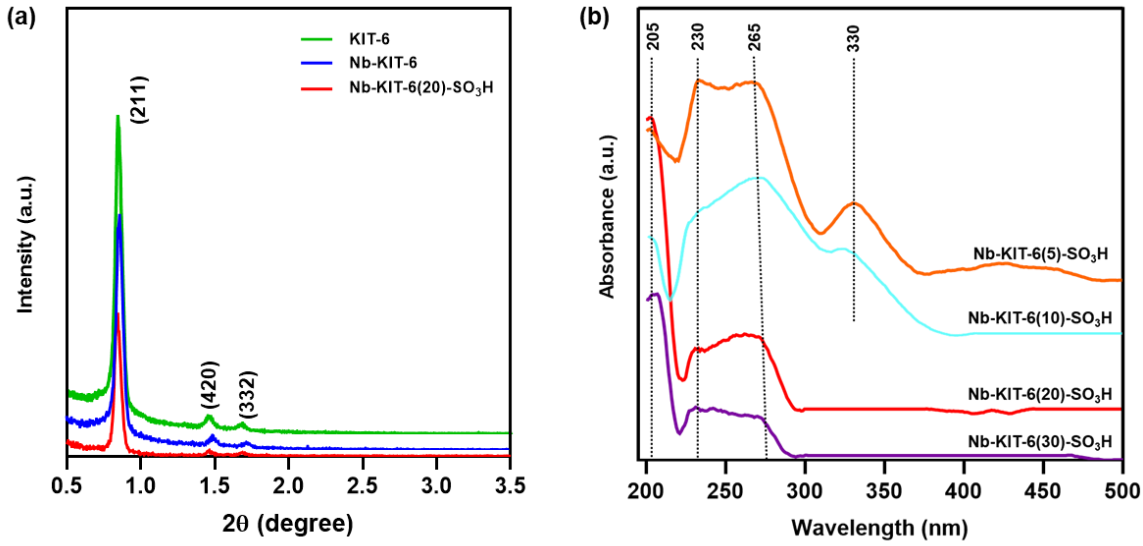


***Fig. 6.4.*** *Small angle X-ray scattering patterns (a) and Diffuse reflectance UV–vis spectra (b) of Nb-KIT-6(x)-$SO_3H$ samples.*

The thermal stability of pristine KIT-6, Nb-KIT-6, and Nb-KIT-6(20)-$SO_3H$ was investigated by TGA analysis (Fig. 6.5). At 80°C, the TGA curves of KIT-6 and Nb-KIT-6 reveal an initial weight loss of 12% owing to the loss of physically adsorbed water

molecules, followed by the loss of firmly adsorbed water molecules with a noncovalent contact with the free sulfonic acid groups. Following that, no significant weight loss was detected in either pure KIT-6 or Nb-KIT-6, indicating that mesoporous silica KIT-6 is thermally stable. After functionalization with sulfonic acid groups, the TGA exhibits a broad peak in the temperature range of 120–220°C with a weight loss of 30.32% which is ascribed to the decomposition of organic moieties of -$SO_3H$ groups functionalized on KIT-6.

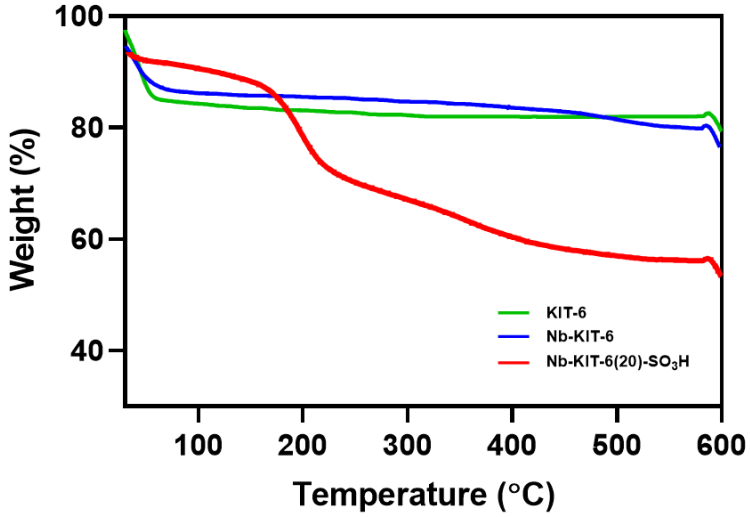


***Fig. 6.5.*** *TGA curves of pure KIT-6, Nb-KIT-6, and Nb-KIT-6(20)-$SO_3H$.*

The porous nature and specific surface area of the samples were investigated by measuring nitrogen adsorption-desorption isotherms and are shown in Fig. 6.6 a. To show the effect of Nb incorporation and sulfonic acid group functionalization we have studied the adsorption-desorption isotherms of KIT-6, Nb-KIT-6, and Nb-KIT-6(x)-$SO_3H$ samples. All the isotherms were classified as type IV, indicating a mesoporous structure. In addition, an H1 hysteresis loop in the isotherm of KIT-6 indicates a well-defined cylindrical pore structure which is observed in all the isotherms and is indicative of the uniformity of pores even after metal incorporation and functionalization that is further confirmed by the pore size distribution curves (Fig. 6.6 b). However, Nb-KIT-6(5)-$SO_3H$ and Nb-KIT-6(10)-$SO_3H$ exhibit a relatively broad hysteresis loop at $P/P_0$ = 0.6-0.9, which also displays a broad pore distribution. This is considered to be due to the formation of small clusters of $Nb_2O_5$ in the mesoporous channels of KIT-6, which affects the KIT-6 structure, as evidenced by high-angle p-XRD and diffuse refraction UV-Vis spectra. Furthermore, the pore size distribution determined by the BJH method seems to have

cylindrical pore geometry, as shown in Table 6.1. With an increase in Nb loading, the BET-specific surface area and total pore volume decreased from 629 to 310 $m^2/g$ and 0.654 to 0.424 $cm^3/g$, respectively. The mean pore diameter calculated using the BJH method is 6.5 nm, and these ordered pore structures were further confirmed by TEM images (Fig. 6.10), which are similar to those seen in other metal-incorporated KIT-6 materials. [21, 22].

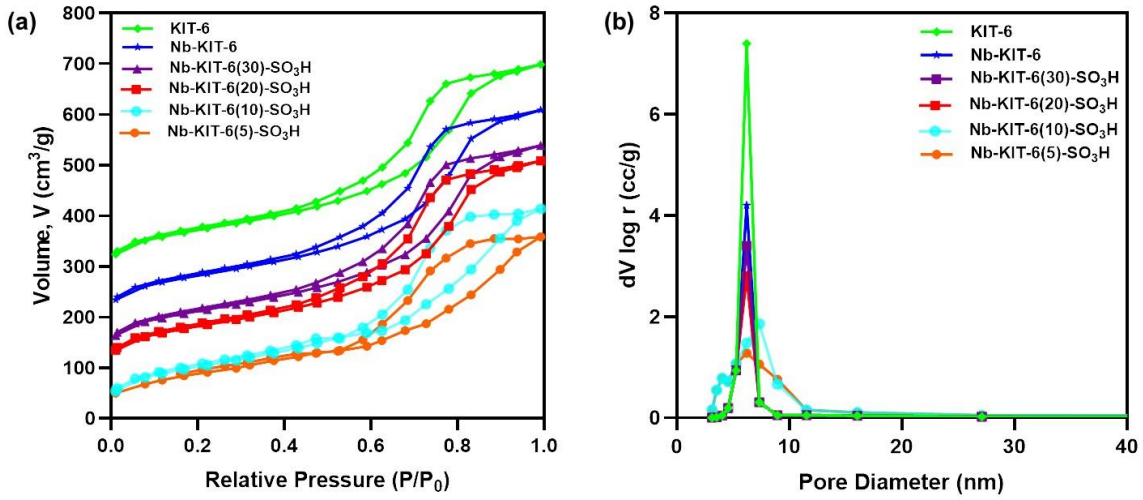


***Fig. 6.6.*** *Nitrogen adsorption-desorption isotherms (a) and the corresponding pore size distribution curves (b) of KIT-6, Nb-KIT-6 with Si/Nb ratio 20, and Nb-KIT-6(x)-$SO_3H$ samples, where x is the Si/Nb ratio.*

***Table 6.1.*** *BET analysis data of KIT-6, Nb-KIT-6 with Si/Nb ratio 20 and Nb-KIT-6(x)-$SO_3H$ samples, where x is the Si/Nb ratio.*

| Catalyst | BET Surface area ($m^2g^{-1}$) | Average pore size (nm) | Total pore volume ($cm^3g^{-1}$) |
|---|---|---|---|
| **KIT-6** | 629 | 3.7 | 0.654 |
| **Nb-KIT-6** | 537 | 3.6 | 0.562 |
| **Nb-KIT-6-(30)-$SO_3H$** | 469 | 3.3 | 0.472 |
| **Nb-KIT-6-(20)-$SO_3H$** | 467 | 3.3 | 0.468 |
| **Nb-KIT-6-(10)-$SO_3H$** | 364 | 3.1 | 0.446 |
| **Nb-KIT-6-(5)-$SO_3H$** | 310 | 2.9 | 0.424 |

The surface acidities of KIT-6, Nb-KIT-6 with Si/Nb ratio 20, and Nb-KIT-6(20)-$SO_3H$ were analyzed by $NH_3$-TPD measurements and the respective results are shown in Fig. 6.7 a. In general, these catalysts have a combination of Lewis and Brönsted acid sites

in the temperature range of 150°C to 400°C [49]. While the acidities of pure KIT-6 without Nb inclusion were very low, the acidities of the Nb-KIT-6 sample were much higher (Fig. 6.7 a). This is because Nb inclusion in silica materials has been shown to produce predominantly Lewis acid sites with a small proportion of Brønsted acid sites [50]. Gaussian peak fitting revealed three peaks for Nb-KIT-6(20)-$SO_3H$, as shown in Fig. 6.7 b. Table 6.2 summarises these findings as well as the overall acidity of the samples. The low-temperature peaks, concentrated around 120–170°C and 200–250°C, have an overall acidity of 0.04–0.08 $NH_3$ mmol/g and are assigned to weak acidic sites of silanol groups (Si-OH). Notably, the majority of the acid sites in all of the samples are of medium acid strength, with the peaks centered at about 350°C. Furthermore, a significant amount of ammonia was desorbed at higher temperatures (538°C), suggesting the presence of strong acidic sites in Nb-KIT-6(20)-$SO_3H$ and is attributed to the sulfonic acid groups (-$SO_3H$) present in the catalyst. The total acidity of Nb-KIT-6(20)-$SO_3H$ catalyst (0.36 $NH_3$ mmol/g) is also markedly higher than those of the Nb-KIT-6 and KIT-6 samples, confirming the successful grafting of sulfonic acid groups in the KIT-6 silica framework. These results are consistent with the results obtained from FT-IR, BET, and TGA as discussed earlier, and XPS, SEM-EDX, and TEM, as discussed in the following paragraphs.

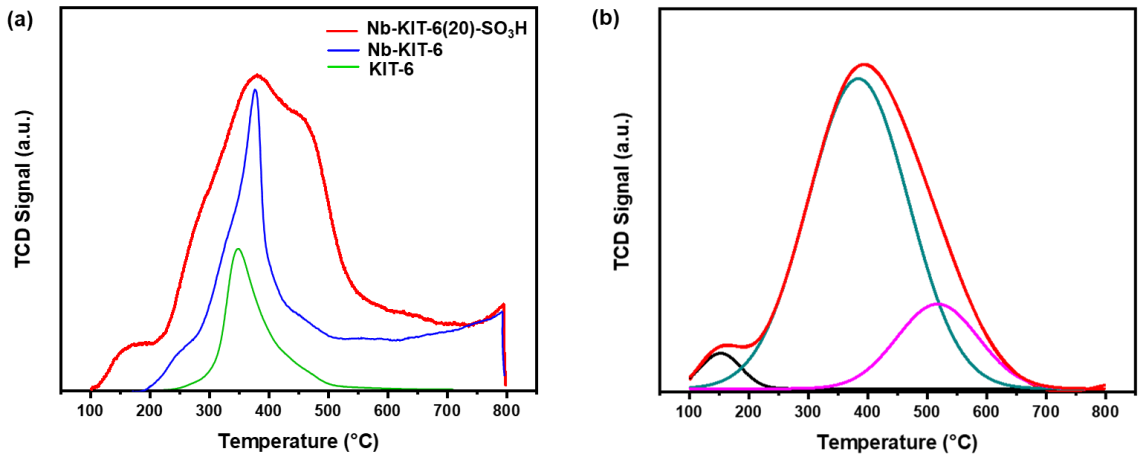


***Fig. 6.7.*** *$NH_3$-TPD analysis of KIT-6, Nb-KIT-6, and Nb-KIT-6(20)-$SO_3H$ (a) and fitting curve of Nb-KIT-6(20)-$SO_3H$ (b).*

***Table 6.2.*** *Total acidity of KIT-6, Nb-KIT-6, and Nb-KIT-6(20)-$SO_3H$.*

| Sample | Total acidity ($NH_3$ mmol/g) | | | |
|---|---|---|---|---|
| | Weak | Moderate | Strong | Total |
| **KIT-6** | 0 | 0.08 | 0 | 0.08 |
| **Nb-KIT-6** | 0.04 | 0.11 | 0 | 0.15 |
| **Nb-KIT-6(20)-$SO_3H$** | 0.08 | 0.17 | 0.11 | 0.36 |

To confirm the formation of Nb-KIT-6(20)-$SO_3H$ catalyst, XPS technique was employed to gain insight into the surface chemical states. The wide-scan survey spectra of Nb-KIT-6(20)-$SO_3H$ (Fig. 6.8 a) shows the distinct peaks at binding energies 532.23 eV, 283.63 eV, 206.8-209.5 eV, 167.62 eV, and 103 eV that are assigned to O (1s), C (1s), Nb (3d), S (2p), and Si (2p), respectively. As shown in Fig. 6.8 b, a well-defined band centered at 103.7 eV is a typical peak of Si (2p) confirming the presence of $SiO_2$ framework. In the deconvoluted Nb (3d) XPS spectra shown in Fig. 6.8 c, two prominent binding energy peaks at 206.2 and 209.0 eV corresponds to the electronic states of Nb ($3d_{5/2}$) and ($3d_{3/2}$), respectively, which are at lower binding energies compared to $Nb_2O_5$ as reported [51]. These results are comparable to previously reported niobium oxide species, which are in agreement with the +4 oxidation state of Nb [51]. The energy difference between these two binding energies is 2.7 eV, indicates that the Nb atoms are extremely well distributed into the KIT-6 silica framework and are linked to silica *via* Si-O-Nb linkage [51]. Thus, from the XPS data it may be concluded that niobium introduced into the KIT-6 silica matrix is an isolated and widely dispersed $NbO_4$ tetrahedral species. All the results mentioned above indicated that the +4-oxidation state of Nb was successfully doped on the KIT-6 framework by the hydrothermal method. The asymmetry of the O (1s) photoelectron peak at binding energy 530.5 eV, shown in Fig. 6.8 d further confirms the presence of Si-O-Nb linkage. In addition, O (1s) spectrum exhibited a higher binding energy peak of O-Si-O linkage at 532.6 eV, which is ascribed to the oxygen atoms that existed as $O^{2-}$ species in the silica framework [52]. The deconvolution of O (1s) peak, as shown in Fig. 6.8 d, also resulted in two more peaks at binding energies 531.6 and 530.6 eV that corresponds to S-O-H and S=O bonds of sulfonic acid groups. The two binding energy peaks at 168.44 and 169.75 eV in the deconvoluted scan of S (2p) (Fig. 6.8 e) are ascribed to $-SO_3^-$ and $-SO_3H$ groups [53], respectively that further confirms the successful sulfate functionalization of the catalyst. The effective grafting of the sulfonic acid groups

on the Nb-KIT6 surface is also established by the deconvoluted C (1s) peaks at 284.9 eV and 286.1 eV (Fig. 6.8 f) which are attributed to C-C and C-S bonds, respectively.

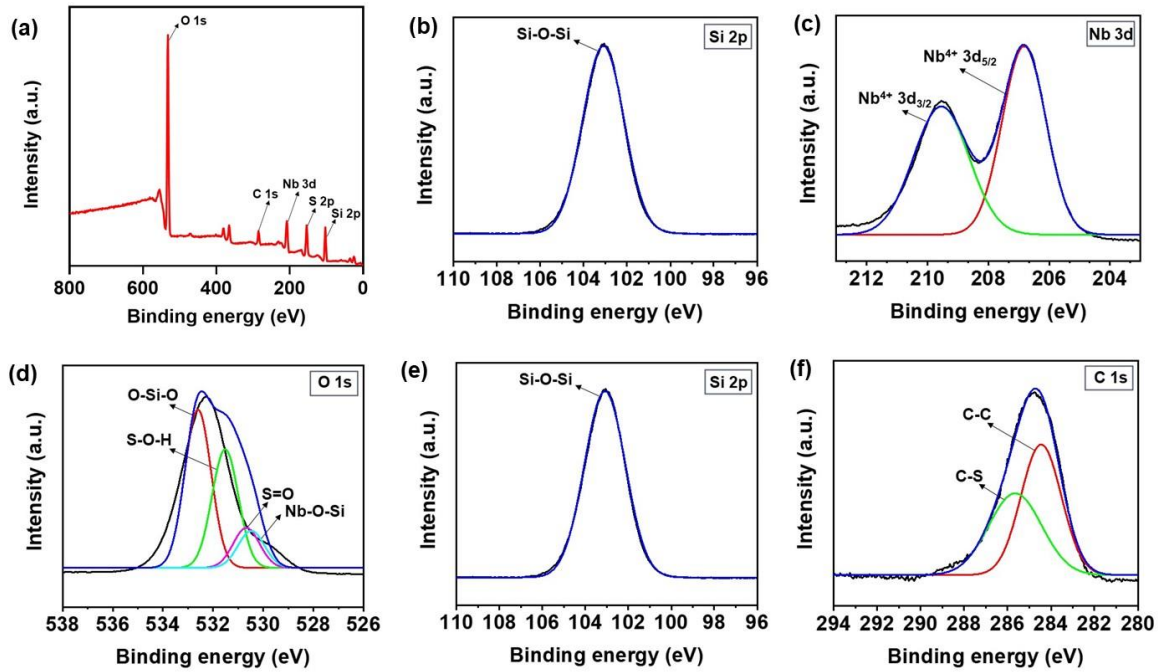


***Fig. 6.8.*** *XPS survey scan of Nb-KIT-6(20)-$SO_3H$ (a); high resolution XPS spectra of Si (2p) (b), Nb (3d) (c), O (1s) (d), S (2p) (e), and C (1s) (f).*

The morphology of the sample particles was investigated by SEM and the images are shown in Fig. 6.9 a, b, and c for KIT-6, Nb-KIT-6, and Nb-KIT-6(20)-$SO_3H$, respectively. The surface of all these materials seems to be somewhat disordered, which is because in most cases, the surface is corrugated rather than terminating along crystallographically well-defined planes. However, in certain segments more regular surface features may be readily seen. To understand the location and distribution of elemental species, EDX analysis was performed and is presented in Fig. 6.9 d, e, and f. The EDX spectrum of KIT-6 (Fig. 6.9 d) exhibits two peaks of Si and O, implying that the sample is composed of a pure silica framework. The EDX pattern of Nb-KIT-6 (Fig. 6.9 e) shows the presence of Nb in addition to Si and O while that of Nb-KIT-6(20)-$SO_3H$ (Fig. 6.9 f) exhibits a peak of S in addition to Si, O, and Nb, confirming the sulfonic acid group functionalization. In addition, the estimated weight percentages and atomic percentages of the samples are tabulated as follows (Fig. 6.9 d, e, and f (insets)). The weight percentages of Nb-KIT-6 and Nb-KIT-6(20)-$SO_3H$ also confirm the Si/Nb ratio to be 20 which is in agreement with our synthesis procedure. Furthermore, the elemental

mapping analysis for the three samples shows a homogeneous distribution of all the elements across the examined region, as shown in Fig. 6.9 g, h for KIT-6, Fig. 6.9 i-k for Nb-KIT-6, and Fig. 6.9 l-o for Nb-KIT-6(20)-$SO_3H$.

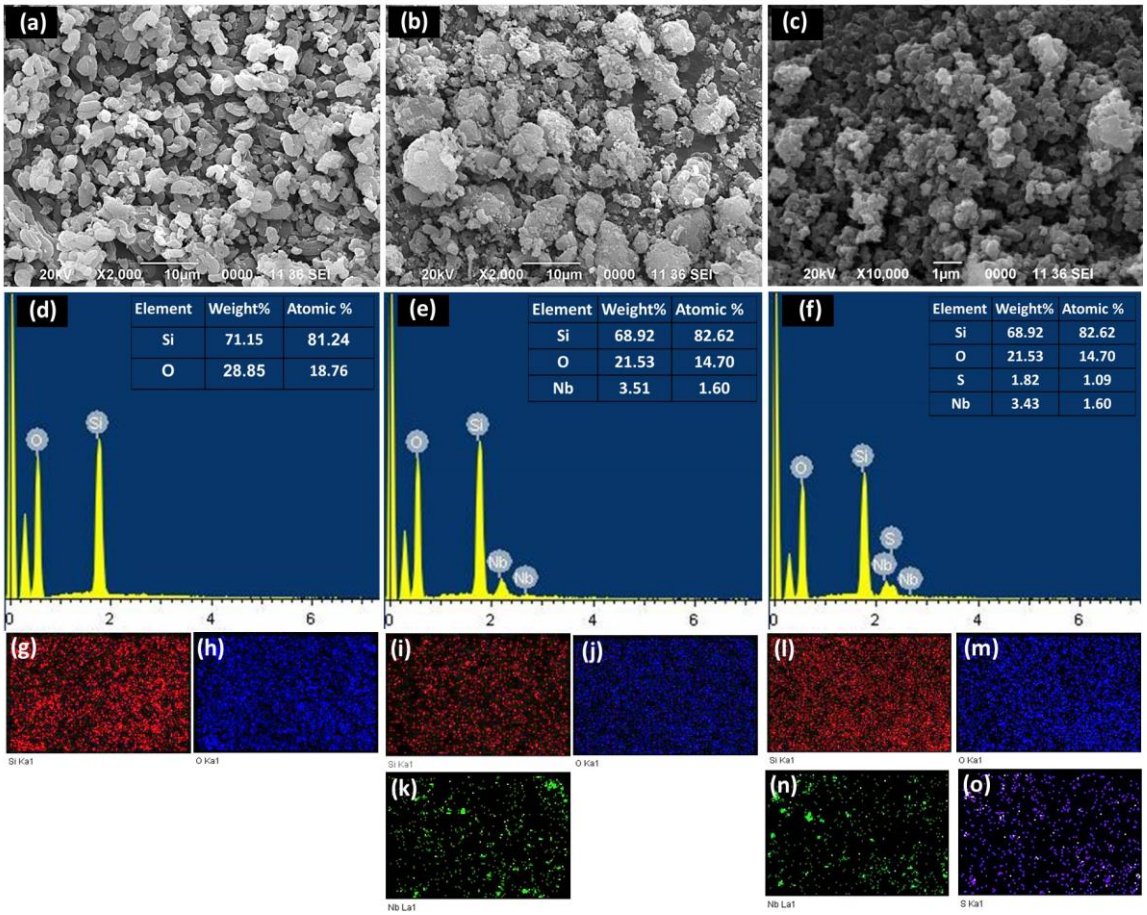


***Fig. 6.9.*** *SEM micrographs of KIT-6 (a), Nb-KIT-6 (b), and Nb-KIT-6(20)-$SO_3H$ (c); EDX spectrum of KIT-6 (d), Nb-KIT-6 (e), and Nb-KIT-6(20)-$SO_3H$ (f); elemental distribution table (d, e and f insets); and pseudo-colour elemental distribution maps of KIT-6 (g, h), Nb-KIT-6 (i-k), and Nb-KIT-6(20)-$SO_3H$ (l-o).*

The representative TEM images of KIT-6 (Fig. 6.10 a, d and g), Nb-KIT-6 (Fig. 6.10 b, e and h), and Nb-KIT-6(20)-$SO_3H$ (Fig. 6.10 c, f and i) are shown at different resolutions. The TEM image of the synthesized KIT-6 (Fig. 6.10 a) revealed that the material has a well-organized 3D cubic pores array with an ordered cubic *Ia3d* symmetric mesoporous structure, which is consistent with the SAXS results. According to the TEM studies of Nb-KIT-6 and Nb-KIT-6(20)-$SO_3H$, the structured mesoporous structure of KIT-6 was sustained even after metal inclusion and post sulfonic-acid group functionalization (Fig. 6.10 b and c). Also, the corresponding pore size distribution histograms of KIT-6, Nb-

KIT-6, and Nb-KIT-6(20)-$SO_3H$ are shown in the insets of Fig. 6.10 a, b, and c, and the observed pore diameters of the samples are compatible with the results of BET analysis.

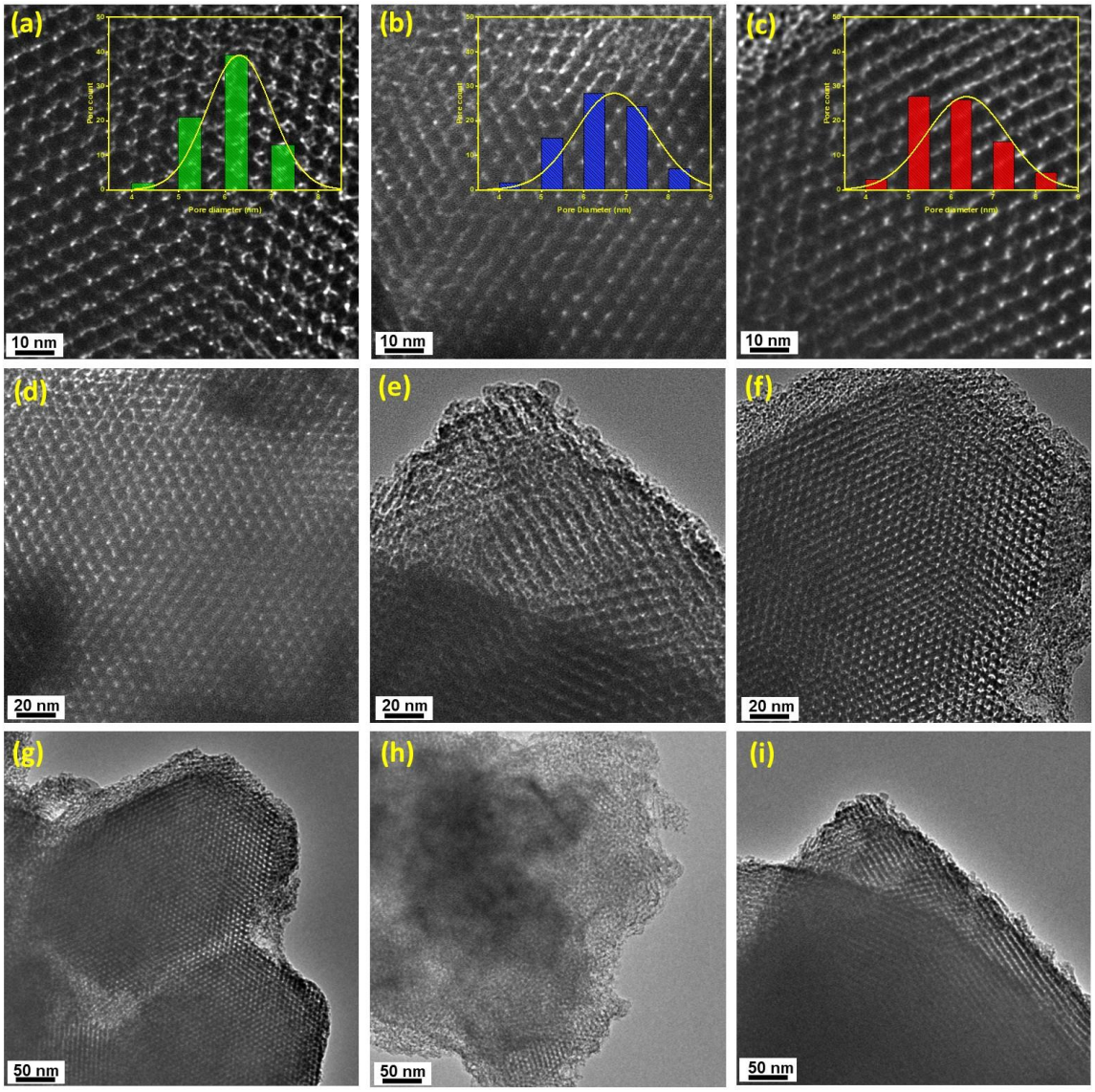


***Fig. 6.10.*** *HRTEM images of KIT-6 (a, d, and g), Nb-KIT-6 (b, e, and h), and Nb-KIT-6(20)-$SO_3H$ (c, f, and i) at 10 nm, 20nm, and 50 nm resolution; the corresponding pore size distribution curves of KIT-6 (a inset), Nb-KIT-6 (d inset) and Nb-KIT-6(20)-$SO_3H$ (g inset).*

### 6.3.3. Optimization of reaction parameters for HMF production using Multivariable Experimental Design

*RSM for modeling and optimization:*

The optimal values of the experimental factors and the effect of their interactions on HMF yield were determined using CCD-based RSM. In our study, the reaction parameters

considered were temperature, reaction time, catalyst loading, and substrate concentration within well-defined boundary conditions with a 95% confidence limit, as shown in Table 6.3. Thus, for optimization of glucose-to-HMF conversion reaction, a five-level-four factor ($5^4$) CCD has been applied that generates 21 sets of reaction conditions. The results obtained corresponding to each experimental run are given in Table 6.4. The following equation represents the empirical relationships between the four variables and the HMF yield by Nb-KIT-6(20)-$SO_3H$:

HMF yield (%) = + 80.79 -7.48 * A -2.01 * B + 3.71 * C -1.46 * D + 0.93 * A * B -2.34 * A * C -1.16 *A * D +1.80 * B * C -7.35 * B * D + 5.36 * C * D -9.03 *$A^2$ -3.91 * $B^2$ -5.70 * $C^2$ -1.74 * $D^2$

Where, A = temperature (°C), B = reaction time (h), C = catalyst loading (mg) and D = substrate concentration (mMol).

***Table 6.3.*** *Coded levels of variables for CCD Response Surface Methodology.*

| Variables | Units | Coded Levels | | | | |
|---|---|---|---|---|---|---|
| | | -α | -1 | 0 | 1 | +α |
| **(A) Temperature** | °C | 120 | 135 | 150 | 165 | 180 |
| **(B) Reaction time** | h | 30 | 45 | 60 | 75 | 90 |
| **(C) Catalyst loading** | mg | 10 | 20 | 30 | 40 | 50 |
| **(D) Substrate concentration** | mMol | 20 | 40 | 60 | 80 | 100 |

The experimental results closely aligned with the predicted outcomes of the reaction conditions. The statistical significance, fit competence, and expected model competency were all assessed using analysis of variance (ANOVA), as shown in Table 6.5. As a consequence, it was considered that the determination coefficient ($R^2$) had a high degree of perfect fit. The predicted $R^2$=0.84 was very near to the expected $R^2$=0.94, indicating that the model was satisfactory. This implies that the RSM prediction model can explain 94% of the entire variation in reaction parameters. Furthermore, the necessary precision of 59 is substantially greater than the standard precision of 4, suggesting that the quadratic model may be utilized to accurately analyze variance in response characteristics [54].

***Table 6.4.*** *CCD and ANN matrix for the four independent variables on the HMF yield with the predicted and actual response.*

| Experimental runs | Temperature (°C) | Reaction time (min) | Catalyst loading (mg) | Substrate concentration (mMol) | HMF Yield % | | | | | |
|---|---|---|---|---|---|---|---|---|---|---|
| | | | | | RSM | | | ANN | | |
| | | | | | Predicted | Observed | Residuals | Predicted | Observed | Residuals |
| **1** | 150 | 30 | 30 | 60 | 62.16 | 69.67 | -7.5 | 70.53 | 69.67 | 0.86 |
| **2** | 150 | 60 | 30 | 60 | 79.79 | 80.07 | -0.3 | 80.77 | 80.07 | 0.70 |
| **3** | 135 | 45 | 20 | 40 | 65.87 | 64.18 | 1.69 | 69.33 | 64.18 | 5.15 |
| **4** | 165 | 75 | 20 | 40 | 64 | 63.31 | 0.69 | 62.56 | 63.31 | -0.75 |
| **5** | 150 | 60 | 10 | 60 | 55.56 | 51.43 | 4.13 | 51.43 | 51.43 | 0.00 |
| **6** | 150 | 60 | 30 | 60 | 83.79 | 80.71 | 3.08 | 80.77 | 80.71 | 0.06 |
| **7** | 150 | 60 | 30 | 60 | 84.79 | 81.48 | 3.31 | 80.77 | 81.48 | -0.71 |
| **8** | 165 | 75 | 40 | 40 | 58.6 | 59.27 | -0.7 | 59.50 | 59.27 | 0.23 |
| **9** | 135 | 75 | 20 | 80 | 45.07 | 43.38 | 1.69 | 43.42 | 43.38 | 0.04 |
| **10** | 135 | 45 | 40 | 40 | 67.64 | 62.31 | 5.33 | 62.31 | 62.31 | 0.00 |
| **11** | 165 | 45 | 20 | 80 | 55.81 | 53.12 | 2.69 | 53.11 | 53.12 | -0.01 |
| **12** | 120 | 60 | 30 | 60 | 59.62 | 60.13 | -0.5 | 60.13 | 60.13 | 0.00 |
| **13** | 180 | 60 | 30 | 60 | 26.71 | 30.22 | -3.5 | 30.47 | 30.22 | 0.25 |
| **14** | 135 | 75 | 40 | 80 | 74.5 | 70.17 | 4.33 | 69.74 | 70.17 | -0.43 |
| **15** | 165 | 45 | 40 | 80 | 64.67 | 63.34 | 1.33 | 63.35 | 63.34 | 0.01 |
| **16** | 150 | 60 | 30 | 60 | 80.79 | 81.36 | -0.6 | 80.77 | 81.36 | -0.59 |
| **17** | 150 | 60 | 30 | 100 | 74.91 | 71.42 | 3.49 | 71.33 | 71.42 | -0.09 |
| **18** | 150 | 60 | 30 | 20 | 74.74 | 77.25 | -2.5 | 77.25 | 77.25 | 0.00 |
| **19** | 150 | 60 | 30 | 60 | 76.79 | 80.32 | -3.5 | 80.77 | 80.32 | 0.45 |
| **20** | 150 | 90 | 30 | 60 | 61.12 | 61.63 | -0.5 | 61.60 | 61.63 | -0.03 |
| **21** | 150 | 60 | 50 | 60 | 67.39 | 65.54 | 1.85 | 65.46 | 65.54 | -0.08 |

The probability (P-value) of the design matrix was examined at a confidence level (α) of 95% using Fischer's statistical test for analysis of variance (ANOVA) (Table 6.6). The model's variance analysis yielded a high F-value (4.73) as well as a very low probability value (< 0.0001). This ensures that the CCD design matrix used in the optimization phase has high significance. According to the fitted single factor interactions based on the CCD-RSM model, the reaction parameters *viz*., temperature, reaction duration, catalyst loading, and substrate concentration substantially impacted the HMF

yield in the glucose to HMF conversion process. AC, BC, BD, CD, $A^2$, $B^2$, $C^2$, and $D^2$, on the other hand, are quadratic connections that have a considerable impact on the HMF yield (Table 6.5). The effect of interaction among the relevant parameters is studied using single-factor interaction plots, as illustrated in Fig. 6.11 a-d. Similarly, significant multivariate 3D interaction plots and their supporting contour plots are shown in Fig. 6.12 a-d and a'-d'. For the single-factor interactions, an increase in the temperature results in a decrease in HMF yield, while an increase in catalyst dosage results in a high HMF yield (Fig. 6.11 a, c). On the other hand, reaction time and substrate concentration are seen to have minor influences on HMF yield, when added within the boundary conditions (Fig. 6.11 b, d). Overall, the impact of the reaction temperature is seen to be highly significant as compared to other reaction parameters.

***Table 6.5.*** *ANOVA for the fitted quadratic polynomial model for HMF yield.*

| Source | Sum of Squares | Degree of Freedom | Mean Square | F value | P-value Prob > F | |
|---|---|---|---|---|---|---|
| **Model** | 3564.12 | 14 | 254.58 | 243.31 | < 0.0001 | S* |
| **A-Temperature** | 447.30 | 1 | 447.30 | 427.51 | < 0.0001 | S |
| **B-Reaction time** | 32.32 | 1 | 32.32 | 30.89 | 0.0014 | S |
| **C-Catalyst** | 219.93 | 1 | 219.93 | 210.20 | < 0.0001 | S |
| **D-Substrate** | 16.99 | 1 | 16.99 | 16.24 | 0.0069 | S |
| **AB** | 3.42 | 1 | 3.42 | 3.27 | 0.1205 | NS# |
| **AC** | 43.90 | 1 | 43.90 | 41.96 | 0.0006 | S |
| **AD** | 5.36 | 1 | 5.36 | 5.12 | 0.0643 | NS |
| **BC** | 25.92 | 1 | 25.92 | 24.77 | 0.0025 | S |
| **BD** | 216.24 | 1 | 216.24 | 206.67 | < 0.0001 | S |
| **CD** | 230.27 | 1 | 230.27 | 220.07 | < 0.0001 | S |
| **A^2** | 2047.21 | 1 | 2047.21 | 1956.61 | < 0.0001 | S |
| **B^2** | 384.25 | 1 | 384.25 | 367.24 | < 0.0001 | S |
| **C^2** | 816.59 | 1 | 816.59 | 780.45 | < 0.0001 | S |
| **D^2** | 76.12 | 1 | 76.12 | 72.75 | 0.0001 | S |
| **Residual** | 6.28 | 6 | 1.05 | | | |
| **Lack of Fit** | 4.73 | 2 | 2.37 | 6.12 | 0.0607 | NS |
| **Pure Error** | 1.55 | 4 | 0.39 | | | |
| **Cor Total** | 3570.40 | 20 | | | | |
| **Std. Dev. = 1.02** | | **Mean = 65.25** | | **Predicted $R^2$ = 0.8414** | | |
| **$R^2$ = 0.9482** | | **Adj. $R^2$ = 0.8841** | | **Adequate Precision = 59.09** | | |

*Significant, #Non-significant

Fig. 6.12 a-d show response surface 3D graphs depicting the impact of multivariate interactions of the Nb-KIT-6(20)-$SO_3H$ catalyst on the glucose-to-HMF conversion process. As demonstrated in the response curve in Fig. 6.12 a, reaction temperature affected HMF synthesis in relation to substrate concentration. Reaction time, on the contrary, was able to affect the HMF yield when used in combination with either catalyst loading (Fig. 6.12 b) or substrate concentration (Fig. 6.12 c). Further, the combination of catalyst loading and substrate concentration shows a notable influence on the HMF yield, wherein 30 mg catalyst loading and 60 mMol of substrate concentration showed the highest yield percentage of 81.36 (Fig. 6.12 d).

Fig. 6.12 a´–d´ shows the contour maps for the foregoing 3D graphs (Fig. 6.12 a-d). A circular contour plot implies that the interactions between the variables are minor, but an elliptical contour plot indicates that the interactions are noteworthy. As the contour plots for the fitted model are elliptical, represented in Fig. 6.12 a´–d´, it reflects that the variables interact significantly [55].

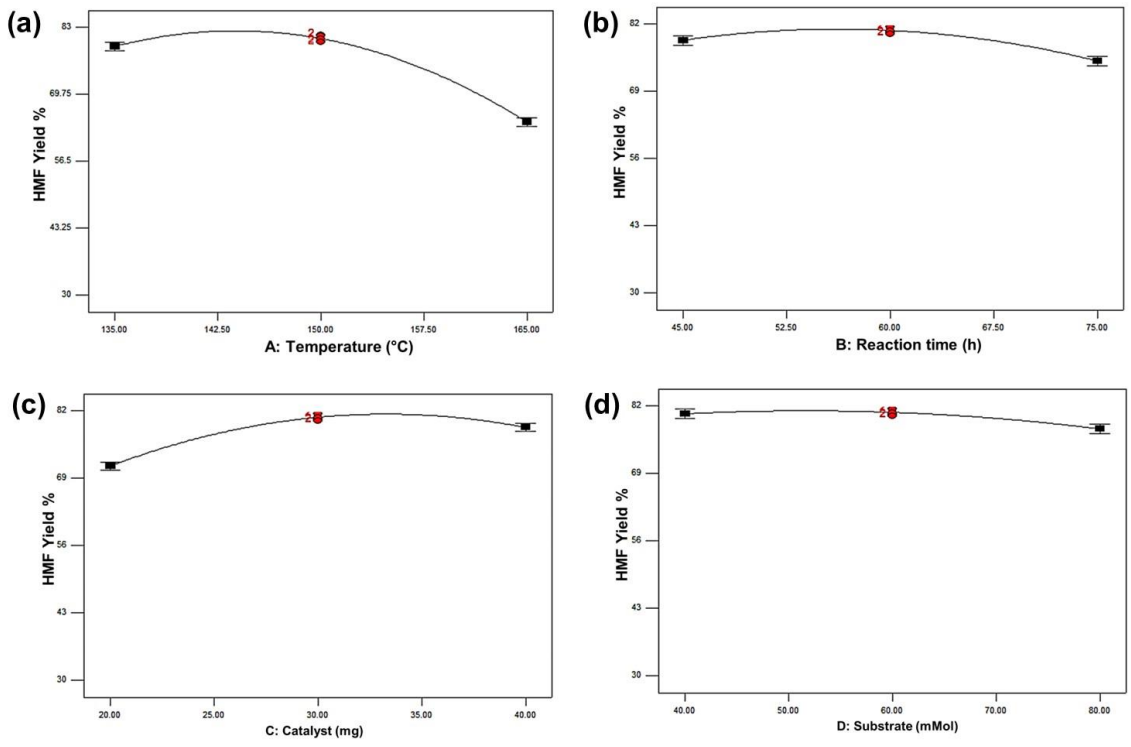


***Fig. 6.11.*** *Effect of univariate interactions defined by the CCD-RSM model on the HMF yield (a-d).*

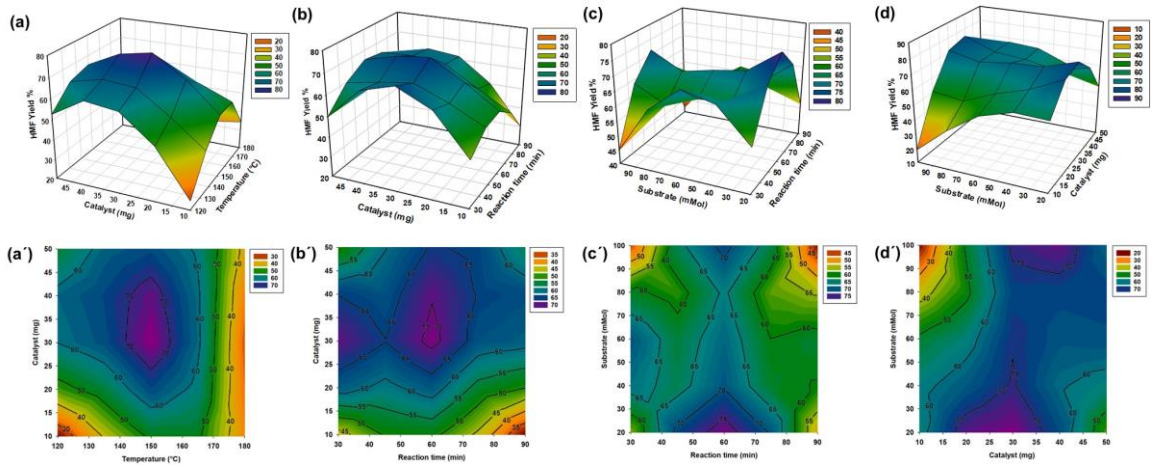


***Fig. 6.12.*** *Effect of multivariate interactions: response surface 3D plots (a-d) and the corresponding contour plots (a´-d´) defined by the CCD-RSM model on the HMF yield.*

A normal probability plot was used to analyze the standard deviation between the predicted and experimental findings to assess the model's adequacy. The normally distributed residuals of the response are depicted in Fig. 6.13 a as a nearly linear distribution of data points forming a straight line. The similarity between the anticipated and actual values is depicted in Fig. 6.13 b. Furthermore, Pareto graphic analysis (Fig. 6.13 c) was performed to determine the percentage effect of the most important factors, with reaction temperature being the most critical element, which is consistent with the findings (Table 6.6).

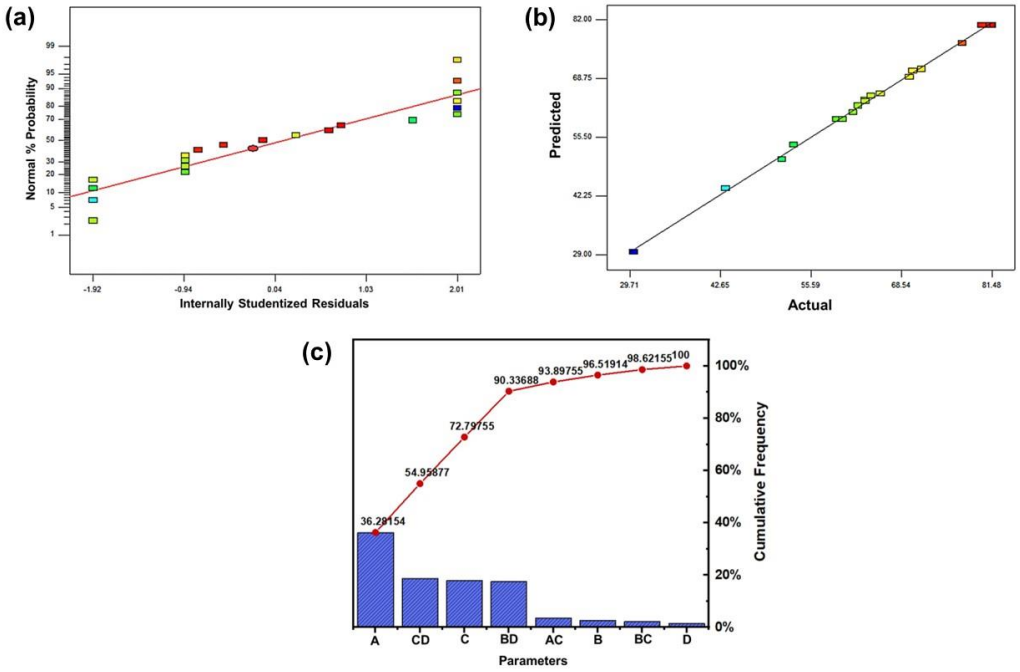


***Fig. 6.13.*** *Normal probability plot (a), predicted vs. actual plot (b), and Pareto graphic analysis described by the model.*

***Table 6.6.*** *Statistical error functions.*

| Error function | Equation | Reference |
|---|---|---|
| **Root mean square error** | $\text{RMSE} = \sqrt{\frac{1}{N}\sum_{i=1}^{N}\left(\frac{P_{R,\exp(i)}-P_{R,cal(i)}}{P_{R,\exp(i)}}\right)^2}$ | [41] |
| **Hybrid fractional error function** | $\text{HYBRID (\%)} = \frac{1}{N-P}\sum\left[\frac{\left(P_{R,i,exp}-P_{R,i,cal}\right)^2}{P_{R,i,exp}}\right]100$ | [56] |
| **Average relative error** | $\text{ARE (\%)} = \frac{100}{N}\sum_{i-1}^{N}\frac{\lvert P_{R,i,exp}-P_{R,i,cal}\rvert}{P_{R,i,exp}}$ | [41] |
| **Absolute average relative error** | $\text{AARE} = \frac{1}{N}\sum_{i=1}^{N}\left(\left\lvert\frac{P_{R,\exp(i)}-P_{R,cal(i)}}{P_{R,\exp(i)}}\right\rvert\right)$ | [56] |
| **Marquardt's percent standard error deviation** | $\text{MPSED (\%)} = \sqrt{\frac{\sum\left(\frac{P_{R,exp}-P_{R,cal}}{P_{R,exp}}\right)^2}{N-P}}\times 100$ | [41] |
| **Correlation coefficient** | $R^2 = \frac{\sum_{i=1}^{N}\left(P_{R,i,cal}-P_{R,exp,ave}\right)^2}{\sum_{i=1}^{N}\left(P_{R,i,cal}-P_{R,exp,ave}\right)^2+\sum_{i=1}^{N}\left(P_{R,i,cal}-P_{R,i,exp}\right)^2}$ | [57] |
| **Adjusted $R^2$** | $\text{Adj } R^2 = 1-\left[(1-R^2)\times\frac{N-1}{N-P-2}\right]$ | [41] |

where N is the number of experimental runs; $P_{R,exp(i)}$, $P_{R,i,exp}$ are the experimental values of the $i^{th}$ experiment; $P_{R,cal(i)}$, $P_{R,i,cal}$ are the model predictions of the $i^{th}$ experiment; $P_{R,exp,ave}$ is the experimentally determined average value, N is the number of experimental runs while P is the number of factors.

*ANN for modeling and optimization:*

The neural network model was pre-processed by normalizing the inputs and targets in the range of 1 to -1 using the 'PREMNMX' function to make training more effective. The input to hidden layer mapping was done with a hyperbolic tangent 'TANSIG' (a sigmoid transfer function), whereas the hidden layer to output layer mapping was done with a purely linear transfer function 'PURELIN'. The data points, which included inputs and their associated outputs, were divided into three random sets to generate the objective model: 70% for constructing the new model, 15% for validation, and the remaining 15% for assessing the model's reliability [40]. The primary step in training a neural network is to design the network's architecture. The number of neurons in the input layer is set by the number of inputs, and the number of neurons in the output layer is fixed by the number of outputs [58]. Furthermore, choosing the best neural network design and topology is crucial for a successful application. Several neural network designs, as well as the number of hidden neurons and learning methods, were investigated for the modeling and prediction of HMF production yield.

Although it is critical to carefully identify the optimal number of hidden neurons based on the type and difficulty of the task, this was often accomplished using a trial-and-error method based on cross-validation. Various network topologies (created by altering the number of nodes in the hidden layer from 1 to 20) are developed using the cross-validation approach. Each one is then trained numerous times and statistically assessed to generate the lowest output error based on the MSE for a validation data set, as shown in Fig. 6.14 a.

The suggested model's regression curve is shown in Fig. 6.14 b, with related values for training, testing, validation, and total data of 0.9996, 0.9703, 0.9900, and 0.9960, respectively. In all data sets, the correlation coefficients were 1, showing that the fit was suitable for all data sets. As a consequence, the ANN output network response was satisfactory in terms of HMF yield prediction accuracy. Table 6.4 displays the total ANN

predicted HMF yield for each response condition as well as the assessment employing the investigational data set.

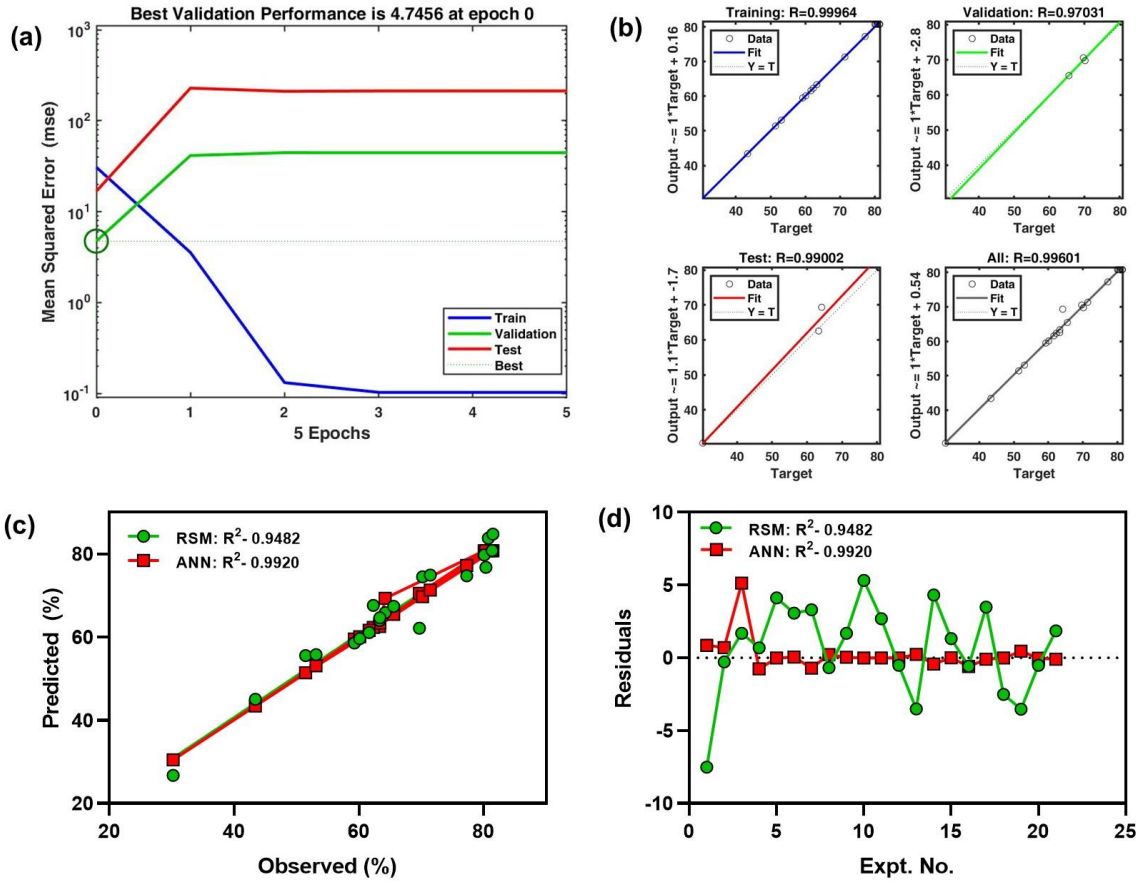


***Fig. 6.14.*** *Selection of the best ANN architecture based on mean squared error (MSE) values (a) and the determination coefficients ($R^2$) (b); comparison of the predictive outputs of RSM and ANN models based on determination coefficients (c) and distribution of residuals (d).*

*Comparison of the RSM and ANN models:*

Comparative evaluations of RSM and ANN have been carried out, and different approaches might be used to assess the goodness and accuracy of a given model, as shown in Table 6.7. $R^2$ is generally used to measure a model's overall predictive capabilities, however, a model's efficiency may not be explained by $R^2$ alone [59]. Apart from $R^2$, adjusted $R^2$ can be implemented to support the accuracy of the model. Adjusted $R^2$ in a multiple linear regression model quantifies the proportion of the variance in the dependent variable explained by the explanatory factors. Adjusted $R^2$ is widely regarded as a more accurate goodness-of-fit statistic than $R^2$. Both $R^2$ and adjusted $R^2$ should be close to 1.

The correlation coefficients for modeling by RSM and ANN were 0.94 and 0.99, respectively, while adjusted $R^2$ were 0.88 and 0.98.

To analyze further the accuracy of the model's prediction, five more statistical error functions, root mean square error (RMSE), average relative error (ARE), absolute average relative error (AARE), hybrid fractional error function (HYBRID), and Marquardt's percent standard error deviation (MPSED) were employed as presented in Table 6.7. In general, the AARE figure should be as low as practical for a good model, while the RMSE value should be near zero. Larger RMSE and AARE values indicate a higher likelihood of prediction errors. In our study, the AARE value (1.12) for RSM was more than twice the AARE value (0.42) for ANN (Table 6.7). Furthermore, the RMSE for RSM (0.203) was greater than the RMSE for ANN (0.014). When compared to the RSM applications, the generated ANN has higher $R^2$ and adjusted $R^2$ values, while the AAD and RMSE values are lower. As a result, ANN outperformed RSM in terms of predictive ability.

***Table 6.7.*** *Statistical error indices of RSM and ANN.*

| **Error function** | **Results** | |
|---|---|---|
| | **RSM** | **ANN** |
| **RMSE** | 0.2032 | 0.0141 |
| **HYBRID (%)** | 0.7014 | 2.8012 |
| **ARE (%)** | 0.4134 | 1.3410 |
| **AARE** | 1.1242 | 0.4216 |
| **MPSED (%)** | 0.9076 | 2.0000 |
| **$R^2$** | 0.9482 | 0.9920 |
| **Adj $R^2$** | 0.8841 | 0.9821 |

### 6.3.4. Experimental validation of RSM and ANN optimal predictive outputs and assessment of the catalytic performance of Nb-KIT-6(20)-$SO_3H$ with lignocellulose (*Saccharum spontaneum* and banana peduncle) derived glucose

The generalization ability can be assessed only with the unseen data set. Therefore, it was decided to test both models and compare the outcomes of the experiments using data set under optimum conditions (Experimental run 7, Table 6.4). The experiments were carried out in triplicate, and the yield of HMF production from the experiment RSM model and ANN model were 79.32% and 80.87%, respectively (Table 6.8).

To validate the catalytic activity of Nb-KIT-6(20)-$SO_3H$ catalyst for the conversion of *Saccharum spontaneum* derived glucose and banana peduncle-derived glucose as discussed in Chapter 2, the reactions are carried out at the optimal reaction condition (60 mMol of glucose with 30 mg catalyst at 150°C for 60 min). To attain 60 mMol of glucose, 112 mg of *Saccharum spontaneum* derived cellulose and banana peduncle-derived cellulose (as discussed in Chapter 1) were subjected to enzymatic hydrolysis using 30 FPU/g of enzyme loading, 5 mg/ml of surfactant concentration and 96 h of incubation time (as discussed in Chapter 2). As predictable, the HMF yields with *Saccharum spontaneum* produced glucose and banana peduncle derived glucose is also much higher, with 78.88% and 79.40%, respectively (Table 6.8), and no byproducts are observed. The HMF peaks in each case are shown in Fig. 6.15 c-f for both aqueous and organic phases, showing glucose peaks with < 10% concentration. The HPLC chromatograms of the aqueous phases, on the other hand, show a peak of furfural of very low concentration for all the substrates including standard glucose, *Saccharum spontaneum* derived glucose, and banana peduncle derived glucose. This may be attributed to the selective conversion of fructose to furfural through dehydration by Lewis's acid sites on $NbO_4$ [60]. However, high HMF selectivity ~85% with > 90% conversion of glucose indicates that the synergistic effect of Nb-KIT-6(20)-$SO_3H$ catalyst and water/MIBK solvent is likely to enhance the glucose conversion and HMF production significantly, inhibiting any condensation byproducts and hydration of HMF in the product mixture.

***Table 6.8.*** *Catalytic conversion of various glucose to HMF with Nb-KIT-6(20)-$SO_3H$ catalyst. Reaction condition: 60 mMol glucose, 30 mg catalyst, 150°C, 60 min.*

| Substrate | Glucose conversion (%) | HMF yield (%) | HMF selectivity (%) |
|---|---|---|---|
| **Standard glucose (optimal RSM condition)** | 92.89 | 79.32 | 85.39 |
| **Standard glucose (optimal ANN condition)** | 94.14 | 80.87 | 85.90 |
| ***Saccharum spontaneum* derived glucose** | 92.34 | 78.88 | 85.42 |
| **Banana peduncle-derived glucose** | 93.56 | 79.40 | 84.86 |

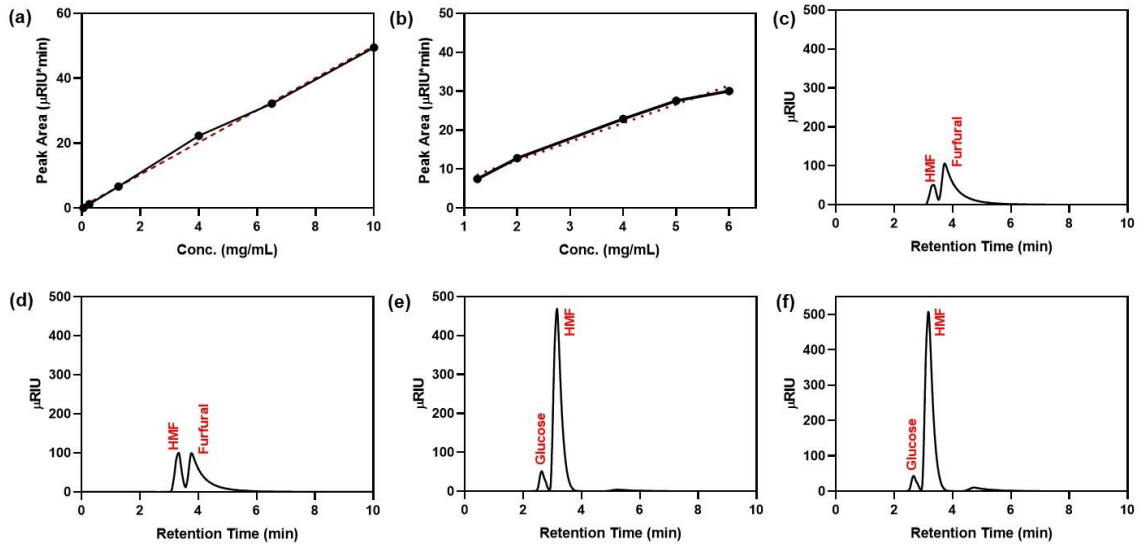


***Fig. 6.15.*** *Glucose standard curve of HPLC (a); HMF standard curve of HPLC (b); HPLC chromatograms showing the HMF peaks in aqueous phase (c, d) and in organic (MIBK) phase (e, f) from Saccharum spontaneum derived glucose and banana peduncle derived glucose, respectively. (Reaction condition: 60 mMol glucose, 30 mg catalyst, 150°C, 60 min).*

### 6.3.5. Recyclability and stability of the catalyst

Catalyst stability is crucial for reducing operation costs in a possibly industrial-scale application. It was reported that typical Lewis's acid catalysts, such as $SnCl_4$ and $TiCl_4$, were readily deactivated and/or degraded under strong hydrothermal conditions, making it difficult to recover and reuse these catalysts after reactions [44]. To resolve this challenge, stability studies of the Nb-KIT-6(20)-$SO_3H$ catalyst were carried out under the optimal conditions (30 mg catalyst, 60 mMol of glucose, 150°C temperature, and 60 min reaction time) for five consecutive cycles. The catalyst recovery procedure is provided in detail in section 6.2.7. After five successive catalytic cycles, only a slight reduction in glucose conversion (from 99.14% to 88.49%) and HMF yield (from 80.87% to 72.51%) was recorded (Fig. 6.16 a). The mechanism underlying the decrease in HMF yield with the increasing number of cycles was investigated using FT-IR (Fig. 6.16 b) and SEM-EDX analysis (Fig. 6.16 c) of fresh and used catalysts. The SEM-EDX study revealed a slight drop in S and Nb content in the fifth used catalyst, which might be the formation of humin in the active sites and/or minor leaching, that leads to a reduction of acidic sites in the catalyst. The SEM-EDX study further revealed a very consistent Nb concentration in the fifth utilized catalyst. Furthermore, in comparison to the fresh catalyst, weak IR peaks

associated with sulfate group characteristics were detected. However, the loss of activity of the catalyst in terms of product yield was only about 6% after five subsequent runs. Therefore, it can be concluded that the developed Nb-KIT-6(20)-$SO_3H$ catalyst in this study might have high reusability and be a very effective and robust solid acid catalyst in the biomass dehydration process. Moreover, the TGA study of the spent catalyst revealed a lower weight loss (22.43%) than that of a fresh catalyst (weight loss of 30.32%) (Fig. 6.16 d). This is most probably due to the lower concentration of sulfonic acid groups in the fifth use catalyst.

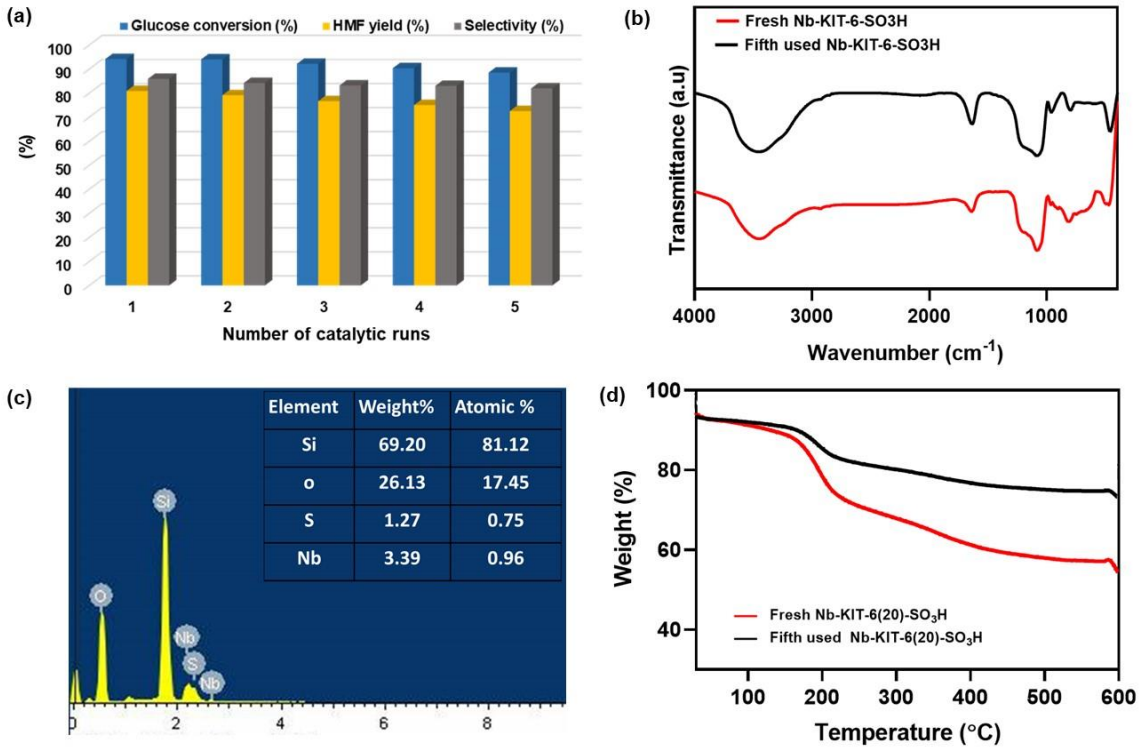


***Fig. 6.16****. Catalyst recycling of Nb-KIT-6(20)-$SO_3H$ (Reaction conditions: 30 mg catalyst, 60 mMol glucose, 150°C, and 60 min) (a), comparison of FTIR spectrum of fresh and fifth used Nb-KIT-6(20)-$SO_3H$ catalyst (b), SEM-EDX spectrum of fifth used Nb-KIT-6(20)-$SO_3H$ catalyst (c), and TGA plots of the fresh and fifth used Nb-KIT-6(20)-$SO_3H$ catalyst (d).*

### 6.3.6. Probable mechanism for the catalytic dehydration of glucose to HMF over Nb-KIT-6(20)-$SO_3H$ catalyst

Based on previous research with bifunctional heterogeneous catalysts, we hypothesized that the glucose-to-HMF conversion over Nb-KIT-6(20)-$SO_3H$ catalyst would also entail two phases, including glucose isomerization to fructose followed by fructose dehydration

to HMF, as shown in Fig. 6.17. Lewis' acid sites are most likely provided by the $NbO_4$ tetrahedral units connected to the silica framework of KIT-6. They interact with glucose to create fructose intermediate by three sequential steps: ring opening, isomerization, and ring-closing. At first, deprotonation of the C1 -OH group and subsequent protonation of the C5 O atom would result in the glucose ring opening. As a result, glucose undergoes a conformational shift, leading to deprotonation by Nb-O. Following that, an intramolecular shift of H from C2 to C1 produces aldose-ketose isomerization, which results in the production of acyclic fructose, which is then followed by a conformational change and H transfer from Nb-OH to the O of C1 to generate cyclic fructose. On the other hand, the -$SO_3H$ groups attached to the silica surface act as Brønsted acid, driving dehydration processes to form HMF *via* H exchange between the catalyst and fructose, releasing three $H_2O$ molecules. The high HMF yield and selectivity obtained in this work Nb- can be attributed to the well-proportioned acid cites in the Nb-KIT-6(20)-$SO_3H$ catalyst attained through niobium incorporation and sulfonic acid group functionalization, as well as the optimized condition obtained through multivariate experimental design.

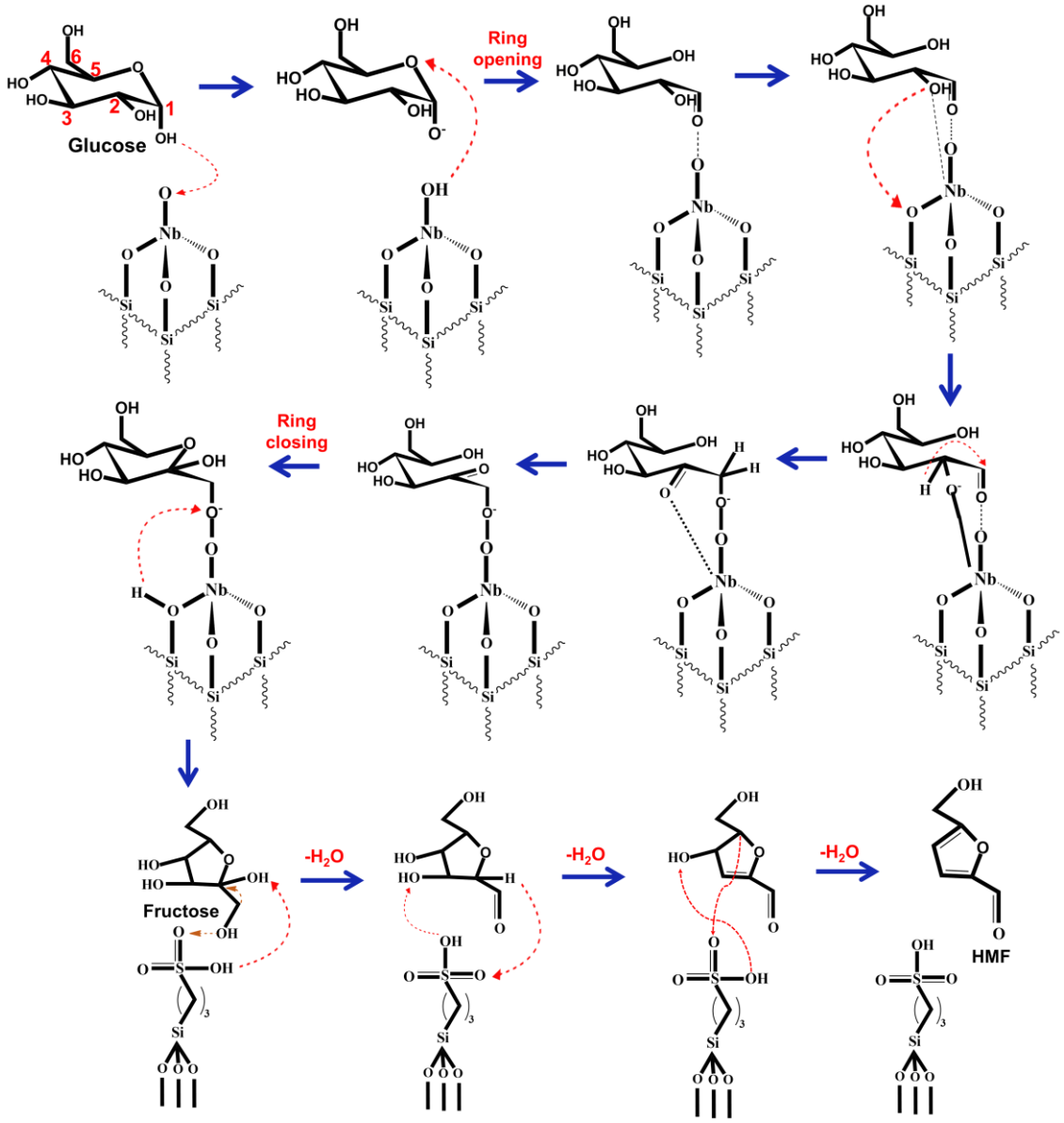


***Fig. 6.17.*** *Proposed mechanism for the catalytic dehydration of glucose to HMF using Nb-KIT-6(20)-$SO_3H$ catalyst.*

## 6.4. Comparison of the activity of Nb-KIT-6(20)-$SO_3H$ with other reported silica-based catalyst

In comparison with other previously reported silica-based catalysts, the Nb-KIT-6(20)-$SO_3H$ catalyst performed better, in terms of HMF yield at optimum reaction temperature and time, as can be seen from Table 6.9. At 170°C and 3 h reaction time in MIBK/$H_2O$ biphasic solvent, Cao et al. reported 34.5% HMF yield using Zirconium doped KIT-6 [19]. In comparison to our catalyst and reaction conditions, a very low yield of HMF was produced at such a high temperature and long reaction time. In a recent study, synthesis of

Niobium doped montmorillonite (Nb-MMT) has been reported resulting in 70.5% HMF yield at 170°C and 3h reaction time in MIBK/$H_2O$-NaCl solvent [61]. Although, high catalytic performance was observed the reaction time was quite high and yield was relatively low as compared to our study. Likewise, MCM-41 and H-ZSM-5 silica-based catalysts exhibited a moderate yield of HMF (~55%) in biphasic MIBK/$H_2O$-NaCl solvent at a very high temperature (195°C) although the reaction time in both the cases was very low (30 min) [19, 62]. Most importantly, in the current study, we have also obtained a high HMF yield with high selectivity from *Saccharum spontaneum* derived glucose and banana peduncle-derived glucose under the developed conditions, as depicted in Table 6.8.

***Table 6.9.*** *Comparison of catalytic performance of Nb-KIT-6(20)-$SO_3H$ with other reported silica-based catalysts.*

| Catalyst | Substrate | Reaction temperature (°C) | Reaction time (min) | Solvent | HMF yield (%) | Reference |
|---|---|---|---|---|---|---|
| **MCM-41** | Glucose | 195 | 30 | MIBK/$H_2O$ -NaCl | 55.8 | [19] |
| **LTL-zeolite** | Glucose | 175 | 90 | MIBK/$H_2O$ | 63.1 | [42] |
| **H-ZSM-5** | Glucose | 195 | 30 | MIBK/$H_2O$ -NaCl | 55.8 | [62] |
| **Nb-MMT** | Glucose | 170 | 180 | MIBK/$H_2O$ -NaCl | 70.5 | [61] |
| **Zr-KIT-6** | Glucose | 170 | 180 | MIBK/$H_2O$ | 34.5 | [45] |
| **H-Mordenite zeolite** | Glucose | 180 | 60 | MIBK/$H_2O$ | 66 | [63] |
| **Nb-KIT-6(20)-$SO_3H$** | Glucose | 150 | 60 | MIBK/$H_2O$ -NaCl | 80.87 | This work |

## 6.5. Conclusion

A well-ordered cubic three-dimensional sulfonated Nb-KIT-6 catalyst with *Ia3d* symmetry with different Si/Nb atomic ratios was successfully synthesized using a hydrothermal synthesis procedure. The catalyst with a Si/Nb atomic ratio of 20 was found to exhibit high efficiency in glucose conversion and HMF production. The presence of a highly ordered cubic structure was revealed by the findings of SAXS, $N_2$ sorption, and high-resolution TEM results. Diffuse reflectance UV–Vis spectra provided direct evidence of Nb species framework inclusion in Nb-KIT-6, and the lack of large crystals of $Nb_2O_5$ was inferred by

high angle p-XRD and diffuse reflectance UV–Vis as well. Furthermore, $NH_3$-TPD measurements reveal that the Nb-KIT-6 sample possesses mostly acid sites of moderate strength, while Nb-KIT-6(20)-$SO_3H$ possesses both moderate and strong acid sites. In addition, the successful grafting of sulfonic acid groups was also confirmed by FTIR, XPS, and SEM-EDX analysis. The as-prepared Nb-KIT-6(20)-$SO_3H$ catalyst showed excellent activity with > 90% glucose conversion and ~80% HMF yield with high HMF selectivity of ~85% after being optimized through CCD-based RSM and MLP-based ANN models in biphasic MIBK/$H_2O$ system. Under optimum reaction conditions, similar catalytic activity was observed for *Saccharum spontaneum* derived glucose and banana peduncle derived glucose. Thus, the acidity of Nb-KIT-6(20)-$SO_3H$ and the biphasic MIBK/$H_2O$ system, both are responsible for the high performance of glucose dehydration to HMF. Comparable yields of the targeted HMF were achieved even after five consecutive cycles. A proposed reaction mechanism over the catalyst was also presented based on the findings. Hence, this work could develop a sustainable way to synthesis highly efficient and stable silica-based solid acids for the dehydration of biomass-derived glucose to HMF.

***References***

[1] Wang, T., Nolte, M. W., and Shanks, B. H. Catalytic dehydration of C 6 carbohydrates for the production of hydroxymethylfurfural (HMF) as a versatile platform chemical. *Green Chemistry*, 16(2):548-572, 2014.

[2] Li, Y., Liu, H., Song, C., Gu, X., Li, H., Zhu, W., Yen, S., and Han, C. The dehydration of fructose to 5-hydroxymethylfurfural efficiently catalyzed by acidic ion-exchange resin in ionic liquid. *Bioresource Technology*, 133:347-353, 2013.

[3] Atanda, L., Silahua, A., Mukundan, S., Shrotri, A., Torres-Torres, G., and Beltramini, J. Catalytic behaviour of $TiO_2$–$ZrO_2$ binary oxide synthesized by sol–gel process for glucose conversion to 5-hydroxymethylfurfural. *RSC Advances*, 5(98):80346-80352, 2015.

[4] Perez, G. P., and Dumont, M. J. Production of HMF in high yield using a low cost and recyclable carbonaceous catalyst. *Chemical Engineering Journal*, 382:122766, 2020.

[5] Zhao, H., Holladay, J. E., Brown, H., and Zhang, Z. C. Metal chlorides in ionic liquid solvents convert sugars to 5-hydroxymethylfurfural. *Science*, 316(5831):1597-1600, 2007.

[6] Hu, S., Zhang, Z., Song, J., Zhou, Y., and Han, B. Efficient conversion of glucose into 5-hydroxymethylfurfural catalyzed by a common Lewis acid $SnCl_4$ in an ionic liquid. *Green Chemistry*, 11(11):1746-1749, 2009.

[7] Kimura, H., Nakahara, M., and Matubayasi, N. In situ kinetic study on hydrothermal transformation of D-glucose into 5-hydroxymethylfurfural through D-fructose with 13C NMR. *The Journal of Physical Chemistry A*, 115(48):14013-14021, 2011.

[8] Yan, H., Yang, Y., Tong, D., Xiang, X., and Hu, C. Catalytic conversion of glucose to 5-hydroxymethylfurfural over $SO_4^{2-}/ZrO_2$ and $SO_4^{2-}/ZrO_2$–$Al_2O_3$ solid acid catalysts. *Catalysis Communications*, 10(11):1558-1563, 2009.

[9] Huber, G. W., Iborra, S., and Corma, A. Synthesis of transportation fuels from biomass: chemistry, catalysts, and engineering. *Chemical Reviews*, 106(9):4044-4098, 2006.

[10] Binder, J. B., Cefali, A. V., Blank, J. J., and Raines, R. T. Mechanistic insights on the conversion of sugars into 5-hydroxymethylfurfural. *Energy & Environmental Science*, 3(6):765-771, 2010.

[11] Jadhav, A. H., Kim, H., and Hwang, I. T. Efficient selective dehydration of fructose and sucrose into 5-hydroxymethylfurfural (HMF) using dicationic room temperature ionic liquids as a catalyst. *Catalysis Communications*, 21:96-103, 2012.

[12] Yang, Y., Liu, W., Wang, N., Wang, H., Li, W., and Song, Z. Effect of Different Ionic Liquids on 5-Hydroxymethylfurfural Preparation from Glucose in DMA over $AlCl_3$: Experimental and Theoretical Study. *Chinese Journal of Chemistry*, 33(5):583-588, 2015.

[13] Bermejo-Deval, R., Assary, R. S., Nikolla, E., Moliner, M., Román-Leshkov, Y., Hwang, S. J., Palsdottir, A., Silverman, D., Lobo, R. F., Curtiss, L. A., and Davis, M. E. Metalloenzyme-like catalyzed isomerizations of sugars by Lewis acid zeolites. *Proceedings of the National Academy of Sciences*, 109(25):9727-9732, 2012.

[14] Yoshida, K., Nanao, H., Kiyozumi, Y., Sato, K., Sato, O., Yamaguchi, A., and Shirai, M. Furfural production from xylose and bamboo powder over chabazite-type zeolite prepared by interzeolite conversion method. *Journal of the Taiwan Institute of Chemical Engineers*, 79:55-59, 2017.

[15] Guo, X., Guo, F., Li, Y., Zheng, Z., Xing, Z., Zhu, Z., Liu, T., Zhang, X., and Jin, Y. Dehydration of D-xylose into furfural over bimetallic salts of heteropolyacid in DMSO/$H_2O$ mixture. *Applied Catalysis A: General*, 558:18-25, 2018.

[16] Antonyraj, C. A., and Haridas, A. A lignin-derived sulphated carbon for acid catalyzed transformations of bio-derived sugars. *Catalysis Communications*, 104:101-105, 2018.

[17] Aellig, C., Scholz, D., Dapsens, P. Y., Mondelli, C., and Pérez-Ramírez, J. When catalyst meets reactor: continuous biphasic processing of xylan to furfural over GaUSY/Amberlyst-36. *Catalysis Science & Technology*, 5(1):142-149, 2015.

[18] Hu, S., Zhu, J., Wu, Y., Xie, R., Wu, K., and Yang, M. Preparation of packing type catalysts AAO@ Al/Meso-$SiO_2$-$SO_3H$ for the dehydration of xylose into furfural. *Microporous and Mesoporous Materials*, 262:112-121, 2018.

[19] Cao, J., Ma, M., Liu, J., Yang, Y., Liu, H., Xu, X., Huang, J., Yue, J., Tian, G., and Feng, S. Highly effective transformation of carbohydrates to 5-Hydroxymethylfurfural with Al-montmorillonite as catalyst. *Applied Catalysis A: General*, 571:96-101, 2019.

[20] Ramanathan, A., Maheswari, R., Barich, D. H., and Subramaniam, B. Niobium incorporated mesoporous silicate, Nb-KIT-6: synthesis and characterization. *Microporous and Mesoporous Materials*, 190:240-247, 2014.

[21] Ramanathan, A., Subramaniam, B., Badloe, D., Hanefeld, U., and Maheswari, R. Direct incorporation of tungsten into ultra-large-pore three-dimensional mesoporous silicate framework: W-KIT-6. *Journal of Porous Materials*, 19(6):961-968, 2012.

[22] Ramanathan, A., Subramaniam, B., Maheswari, R., and Hanefeld, U. Synthesis and characterization of Zirconium incorporated ultra large pore mesoporous silicate, Zr–KIT-6. *Microporous and Mesoporous Materials*, 167:207-212, 2013.

[23] Kleitz, F., Berube, F., Guillet-Nicolas, R., Yang, C. M., and Thommes, M. Probing adsorption, pore condensation, and hysteresis behavior of pure fluids in three-dimensional cubic mesoporous KIT-6 silica. *The Journal of Physical Chemistry C*, 114(20):9344-9355, 2010.

[24] Jiang, C., Zhu, J., Wang, B., Li, L., and Zhong, H. One-pot synthesis of 5-hydroxymethylfurfural from glucose over zirconium doped mesoporous KIT-6. *Chinese Journal of Chemical Engineering*, 26(6):1270-1277, 2018.

[25] Jaswal, A., Singh, P. P., and Mondal, T. Furfural–a versatile, biomass-derived platform chemical for the production of renewable chemicals. *Green Chemistry*, 24(2):510-551, 2022.

[26] Sumiya, S., Oumi, Y., Sadakane, M., and Sano, T. Facile preparation of SBA-15-supported niobic acid ($Nb_2O_5 \cdot nH_2O$) catalyst and its catalytic activity. *Applied Catalysis A: General*, 365(2):261-267, 2009.

[27] Malihan, L. B., Nisola, G. M., Mittal, N., Lee, S. P., Seo, J. G., Kim, H., and Chung, W. J. SBA-15 supported ionic liquid phase (SILP) with $H_2PW_{12}O_{40}$− for the hydrolytic catalysis of red macroalgal biomass to sugars. *RSC Advances*, 6(40):33901-33909, 2016.

[28] Anilkumar, M., and Hölderich, W. F. Highly active and selective Nb modified MCM-41 catalysts for Beckmann rearrangement of cyclohexanone oxime to ε-caprolactam. *Journal of Catalysis*, 260(1):17-29, 2008.

[29] Yan, W., Wu, Y., Feng, X., Yang, C., Jin, X., and Shen, J. Selective propylene epoxidation in liquid phase using highly dispersed Nb catalysts incorporated in mesoporous silicates. *Chinese Journal of Chemical Engineering*, 26(6):1278-1284, 2018.

[30] Somma, F., and Strukul, G. Niobium containing micro-, meso-and macroporous silica materials as catalysts for the epoxidation of olefins with hydrogen peroxide. *Catalysis Letters*, 107(1):73-81, 2006.

[31] Yan, W., Zhang, G., Yan, H., Liu, Y., Chen, X., Feng, X., Jin, X., and Yang, C. Liquid-phase epoxidation of light olefins over W and Nb nanocatalysts. *ACS Sustainable Chemistry & Engineering*, 6(4):4423-4452, 2018.

[32] Sobczak, I., Kieronczyk, N., Trejda, M., and Ziolek, M. Gold, vanadium and niobium containing MCM-41 materials—Catalytic properties in methanol oxidation. *Catalysis Today*, 139(3):188-195, 2008.

[33] Hu, L., Tang, X., Wu, Z., Lin, L., Xu, J., Xu, N., and Dai, B. Magnetic lignin-derived carbonaceous catalyst for the dehydration of fructose into 5-hydroxymethylfurfural in dimethylsulfoxide. *Chemical Engineering Journal*, 263:299-308, 2015.

[34] Moreno-Recio, M., Santamaría-González, J., and Maireles-Torres, P. Brönsted and Lewis acid ZSM-5 zeolites for the catalytic dehydration of glucose into 5-hydroxymethylfurfural. *Chemical Engineering Journal*, 303:22-30, 2016.

[35] Zhang, Z., Song, J., and Han, B. Catalytic transformation of lignocellulose into chemicals and fuel products in ionic liquids. *Chemical Reviews*, 117(10):6834-6880, 2017.

[36] Mohammadbagheri, Z., and Chermahini, A. N. KCC-1/Pr-$SO_3H$ as an efficient heterogeneous catalyst for production of n-butyl levulinate from furfuryl alcohol. *Journal of Industrial and Engineering Chemistry*, 62:401-408, 2018.

[37] Kaiprommarat, S., Kongparakul, S., Reubroycharoen, P., Guan, G., and Samart, C. Highly efficient sulfonic MCM-41 catalyst for furfural production: Furan-based biofuel agent. *Fuel*, 174:189-196, 2016.

[38] Rai, S. K., and Mukherjee, A. K. Statistical optimization of production, purification and industrial application of a laundry detergent and organic solvent-stable subtilisin-like serine protease (Alzwiprase) from *Bacillus subtilis* DM-04. *Biochemical Engineering Journal*, 48:173-180, 2010.

[39] Roy, J. K., Rai, S. K., and Mukherjee, A. K. Characterization and application of a detergent-stable alkaline α-amylase from *Bacillus subtilis* strain AS-S01a. *International Journal of Biological Macromolecules*, 50:219-229, 2012.

[40] Baruah, J., Chaliha, C., Kalita, E., Nath, B. K., Field, R. A., and Deb, P. Modelling and optimization of factors influencing adsorptive performance of agrowaste-derived

Nanocellulose Iron Oxide Nanobiocomposites during remediation of Arsenic contaminated groundwater. *International Journal of Biological Macromolecules*, 164:53-65, 2020.

[41] Onu, C. E., Nwabanne, J. T., Ohale, P. E., and Asadu, C. O. Comparative analysis of RSM, ANN and ANFIS and the mechanistic modeling in eriochrome black-T dye adsorption using modified clay. *South African Journal of Chemical Engineering*, 36:24-42, 2021

[42] Dias, A. S., Lima, S., Carriazo, D., Rives, V., Pillinger, M., and Valente, A. A. Exfoliated titanate, niobate and titanoniobate nanosheets as solid acid catalysts for the liquid-phase dehydration of D-xylose into furfural. *Journal of Catalysis*, 244(2):230-237, 2006.

[43] Qiu, G., Huang, C., Sun, X., and Chen, B. Highly active niobium-loaded montmorillonite catalysts for the production of 5-hydroxymethylfurfural from glucose. *Green Chemistry*, 21(14):3930-3939, 2019.

[44] Cai, W., Chen, Q., Xuan, H., Li, C., Yu, H., Cui, L., Yu, Z., Zhang, S., and Qu, F. One-pot synthesis of lactic acid from cellulose over a sulfonated Sn-KIT6 catalyst. *Korean Journal of Chemical Engineering*, 36(4):513-521, 2019.

[45] Cao, H. X., Zhang, J., Guo, C. L., Chen, J. G., and Ren, X. K. Highly dispersed Ni nanoparticles on 3D-mesoporous KIT-6 for CO methanation: Effect of promoter species on catalytic performance. *Chinese Journal of Catalysis*, 38(7):1127-1137, 2017.

[46] Liu, J., Xue, D., and Li, K. Single-crystalline nanoporous $Nb_2O_5$ nanotubes. *Nanoscale Research Letters*, 6(1):1-8, 2011.

[47] Li, L., Zhou, P., Zhang, H., Meng, X., Li, J., and Sun, T. Mid-temperature deep removal of hydrogen sulfide on rare earth (RE= Ce, La, Sm, Gd) doped ZnO supported on KIT-6: Effect of RE dopants and interaction between active phase and support matrix. *Applied Surface Science*, 407:197-208, 2017.

[48] Zhao, X., Huang, L., Li, H., Hu, H., Hu, X., Shi, L., and Zhang, D. Promotional effects of zirconium doped CeVO4 for the low-temperature selective catalytic reduction of NOx with NH3. *Applied Catalysis B: Environmental*, 183:269-281, 2016.

[49] Wang, J., Ren, J., Liu, X., Lu, G., and Wang, Y. High yield production and purification of 5-hydroxymethylfurfural. *AIChE Journal*, 59(7):2558-2566, 2013.

[50] Trejda, M., Tuel, A., Kujawa, J., Kilos, B., and Ziolek, M. Niobium rich SBA-15 materials–preparation, characterisation and catalytic activity. *Microporous and Mesoporous Materials*, 110(2-3):271-278, 2008.

[51] Ofoegbuna, T., Darapaneni, P., Sahu, S., Plaisance, C., and Dorman, J. A. Stabilizing the B-site oxidation state in ABO 3 perovskite nanoparticles. *Nanoscale*, 11(30):14303-14311, 2019.

[52] Gopinath, S., Kumar, P. S. M., Arafath, K. Y., Thiruvengadaravi, K. V., Sivanesan, S., and Baskaralingam, P. Efficient mesoporous $SO_4^{2-}$/Zr-KIT-6 solid acid catalyst for green diesel production from esterification of oleic acid. *Fuel*, 203:488-500, 2017.

[53] Zheng, L., Xiong, L., Liu, C., and Jin, L. Electrochemical synthesis of a novel sulfonated polyaniline and its electrochemical properties. *European Polymer Journal*, 42(10):2328-2333, 2006.

[54] Liu, W., Ji, J., Chen, H., and Ye, C. Optimal color design of psychological counselling room by design of experiments and response surface methodology. *PloS one*, 9(3):e90646, 2014.

[55] Shang, H., Zhou, H., Duan, M., Li, R., Wu, H., and Lou, Y. Extraction condition optimization and effects of drying methods on physicochemical properties and antioxidant activities of polysaccharides from comfrey (*Symphytum officinale* L.) root. *International Journal of Biological Macromolecules*, 112:889-899, 2018.

[56] Ayawei, N., Ebelegi, A. N., and Wankasi, D. Modelling and interpretation of adsorption isotherms. *Journal of Chemistry*, 2017:1-11, 2017.

[57] Wakkel, M., Khiari, B., and Zagrouba, F. Textile wastewater treatment by agro-industrial waste: equilibrium modelling, thermodynamics and mass transfer mechanisms of cationic dyes adsorption onto low-cost lignocellulosic adsorbent. *Journal of Taiwan Institute of Chemical Engineers*, 96:439-452, 2019.

[58] Rafigh, S. M., Yazdi, A. V., Vossoughi, M., Safekordi, A. A., and Ardjmand, M. Optimization of culture medium and modeling of curdlan production from *Paenibacillus polymyxa* by RSM and ANN. *International Journal of Biological Macromolecules*, 70:463-473, 2014.

[59] Ebrahimpour, A., Rahman, R. N. Z. R. A., Ean Ch'ng, D. H., Basri, M., and Salleh, A. B. A modeling study by response surface methodology and artificial neural network on culture parameters optimization for thermostable lipase production from

a newly isolated thermophilic *Geobacillus* sp. strain ARM. *BMC biotechnology*, 8(1):1-15, 2008.

[60] Gupta, N. K., Fukuoka, A., and Nakajima, K. Amorphous $Nb_2O_5$ as a selective and reusable catalyst for furfural production from xylose in biphasic water and toluene. *ACS Catalysis*, 7(4):2430-2436, 2017.

[61] Zhu, Y., Xu, X., He, J., Guo, J., and Song, K. Effective dehydration of fructose over stable Ti-doped SBA-15 catalysts. *Frontiers in Chemistry*, 9:817417, 2021.

[62] Moreno-Recio, M., Jiménez-Morales, I., Arias, P. L., Santamaría-González, J., and Maireles-Torres, P. The Key Role of Textural Properties of Aluminosilicates in the Acid-Catalysed Dehydration of Glucose into 5-Hydroxymethylfurfural. *ChemistrySelect*, 2(8):2444-2451, 2017.

[63] Velaga, B., and Peela, N. R. Seed-assisted and OSDA-free synthesis of H-mordenite zeolites for efficient production of 5-hydroxymethylfurfural from glucose. *Microporous and Mesoporous Materials*, 279:211-219, 2019.